

BASS XLV: Quantifying AGN Selection Effects in the Chandra COSMOS-Legacy Survey with BASS

YARONE M. TOKAYER,¹ MICHAEL J. KOSS,² C. MEGAN URRY,³ PRIYAMVADA NATARAJAN,³ RICHARD MUSHOTZKY,^{4,5}
MISLAV BALOKOVIĆ,³ FRANZ E. BAUER,^{6,7,8} PETER BOORMAN,⁹ ALESSANDRO PECA,^{10,2,1} CLAUDIO RICCI,^{11,12}
FEDERICA RICCI,¹³ DANIEL STERN,¹⁴ EZEQUIEL TREISTER,¹⁵ AND BENNY TRAKHTENBROT¹⁶

¹*Department of Physics, Yale University, P.O. Box 208121, New Haven, CT 06520, USA*

²*Eureka Scientific, 2452 Delmer Street Suite 100, Oakland, CA 94602-3017, USA*

³*Yale Center for Astronomy & Astrophysics and Department of Physics, Yale University, P.O. Box 208120, New Haven, CT 06520-8120, USA*

⁴*Department of Astronomy, University of Maryland, College Park, MD 20742, USA*

⁵*Joint Space-Science Institute, University of Maryland, College Park, MD 20742, USA*

⁶*Instituto de Astrofísica and Centro de Astroingeniería, Facultad de Física, Pontificia Universidad Católica de Chile, Casilla 306, Santiago 22, Chile*

⁷*Millennium Institute of Astrophysics (MAS), Nuncio Monseñor Sótero Sanz 100, Providencia, Santiago, Chile*

⁸*Space Science Institute, 4750 Walnut Street, Suite 205, Boulder, Colorado 80301, USA*

⁹*Cahill Center for Astronomy and Astrophysics, California Institute of Technology, Pasadena, CA 91125, USA*

¹⁰*Department of Physics, University of Miami, Coral Gables, FL 33124, USA*

¹¹*Instituto de Estudios Astrofísicos, Facultad de Ingeniería y Ciencias, Universidad Diego Portales, Av. Ejército Libertador 441, Santiago, Chile*

¹²*Kavli Institute for Astronomy and Astrophysics, Peking University, Beijing 100871, People's Republic of China*

¹³*Dipartimento di Fisica e Astronomia, Università di Bologna, via Gobetti 93/2, 40129 Bologna, Italy*

¹⁴*Jet Propulsion Laboratory, California Institute of Technology, 4800 Oak Grove Drive, MS 169-224, Pasadena, CA 91109, USA*

¹⁵*Instituto de Astrofísica, Facultad de Física, Pontificia Universidad Católica de Chile, Casilla 306, Santiago 22, Chile*

¹⁶*School of Physics and Astronomy, Tel Aviv University, Tel Aviv 69978, Israel*

ABSTRACT

Deep extragalactic X-ray surveys, such as the Chandra COSMOS-Legacy field (CCLS), are prone to be biased against active galactic nuclei (AGN) with high column densities due to their lower count rates at a given luminosity. To quantify this selection effect, we forward model nearby ($z \sim 0.05$) AGN from the BAT AGN Spectroscopic Survey (BASS) with well-characterized ($\gtrsim 1000$ cts) broadband X-ray spectra (0.5–195 keV) to simulate the CCLS absorption distribution. We utilize the BASS low-redshift analogs with similar luminosities to the CCLS ($L_{2-10 \text{ keV}}^{\text{int}} \sim 10^{42-45} \text{ erg s}^{-1}$), which are much less affected by obscuration and low-count statistics, as the seed for our simulations, and follow the spectral fitting of the CCLS. Our simulations reveal that Chandra would fail to detect the majority (53.3%; 563/1056) of obscured ($N_{\text{H}} \geq 10^{22} \text{ cm}^{-2}$) simulated BASS AGN given the observed redshift and luminosity distribution of the CCLS. Even for detected sources with sufficient counts (≥ 30) for spectral modeling, the level of obscuration is significantly overestimated. This bias is most extreme for objects whose best fit indicates a high-column density AGN ($N_{\text{H}} \geq 10^{24} \text{ cm}^{-2}$), since the majority (66.7%; 18/27) of these are actually unobscured sources ($N_{\text{H}} < 10^{22} \text{ cm}^{-2}$). This implies that previous studies may have significantly overestimated the increase in the obscured fraction with redshift and the fraction of luminous obscured AGN. Our findings highlight the importance of directly considering obscuration biases and forward modeling in X-ray surveys, as well as the need for higher-sensitivity X-ray missions such as the Advanced X-ray Imaging Satellite (AXIS), and the importance of multi-wavelength indicators to estimate obscuration in distant supermassive black holes.

1. INTRODUCTION

Active galactic nuclei (AGN)—luminous galactic centers powered by accreting supermassive black holes (SMBHs)—are powerful probes of the nature of black hole growth, galactic evolution, and cosmology. During

the course of their lifetimes, the Chandra X-ray Observatory and XMM-Newton have observed over 50 extragalactic survey fields at depths of up to ~ 7 Ms that cumulatively add up to years of observing time (Brandt & Hasinger 2005; Brandt & Alexander 2015). This has led to the discovery of thousands of distant black holes as AGN, and enabled resolving most of the cosmic X-ray background below 10 keV (Gilli et al. 2007; Treister et al. 2009; Brandt & Yang 2022). However, surveys with “soft” X-ray telescopes ($E < 10$ keV) remain highly biased against heavily obscured AGN (e.g., Burlon et al. 2011), whose spectra peak at 20–30 keV (Brightman & Nandra 2011; Ricci et al. 2015; Koss et al. 2016).

AGN are believed to contain a torus of obscuring gas and dust, which can lead to significant attenuation of much of their electromagnetic spectra (Hickox & Alexander 2018), depending on the viewing angle (e.g., Elvis 2000; Urry 2004), intrinsic luminosity (Duras et al. 2020; Caglar et al. 2020), Eddington ratio (Ricci et al. 2017a, 2022, 2023a; Caglar et al. 2023), the nature of the host galaxy (Koss et al. 2011, 2021), and possibly the cosmological epoch (Franca et al. 2005; Akylas et al. 2006; Hasinger 2008; Peca et al. 2023; Matthee et al. 2024). Detecting and characterizing the AGN population is critical to obtaining a fuller census of SMBHs and active galaxies across cosmic time. They are also of particular interest since these optically-thick environments can be the result of galaxy mergers (e.g., Koss et al. 2010, 2012; Ricci et al. 2017b; Koss et al. 2018; Ricci et al. 2021), which are believed to play a critical role in triggering AGN activity and serve as an important growth channel for both SMBHs and the galaxies in which they reside (e.g., Hopkins et al. 2006).

AGN obscuration is quantified by the column density of obscuring material along the line of sight, N_{H} , which includes obscuration near the SMBH in the torus and farther out in the host galaxy in which it resides. We refer to sources with $N_{\text{H}} \geq 10^{22}$ cm $^{-2}$ as “obscured” and those with $N_{\text{H}} \geq 10^{24}$ cm $^{-2}$ as “Compton-thick” (CT). In many well-studied objects, the presence of this obscuring material significantly reduces the AGN’s soft X-ray, optical, and UV signatures. There are two spectral bands, the ultra-hard X-ray ($E > 10$ keV) and mid-IR (5–50 μm), that are less sensitive to the effects of obscuration and thus can survey a wide range of AGN where this obscuring material is optically thin up to the CT regime (e.g., Koss et al. 2013; Ricci et al. 2015).

Recently, results from ALMA have suggested that nuclear millimeter emission may also be used effectively to detect highly obscured nearby AGN (Kawamuro et al. 2022; Ricci et al. 2023b). While it is also insensitive to obscuration, strong lower frequency radio emission

is found only in a fraction of AGN (Wilson & Colbert 1995). Weaker radio emission in the GHz band was found in the majority of BASS AGN at 1–2” scales (Smith et al. 2020), but has a much larger scatter with the X-ray emission (~ 1 dex) than in the millimeter band.

While mid-IR selection is reliable in identifying very luminous AGN where nuclear emission is dominant, moderate luminosity AGN, such as those commonly found in the local Universe, are not easily identified because of host galaxy contamination (e.g., Ichikawa et al. 2017). Importantly, host contamination becomes more problematic for $z \gtrsim 0.5$, since the typical star forming galaxies detected at those cosmic epochs appear as luminous infrared galaxies (“LIRGs”) (e.g., Madau & Dickinson 2014). In contrast, X-ray surveys suffer little contamination from non-nuclear emission at typical survey depths and can therefore successfully find both low- and high-luminosity AGN (Koss et al. 2022a). Ultra-hard X-ray surveys performed by the Swift/BAT instrument (14–195 keV; Barthelmy et al. 2005) and more recently by NuSTAR (Harrison et al. 2013), have played a critical role in identifying low-luminosity, heavily obscured AGN in the local universe. (e.g., Kawamuro et al. 2016; Lansbury et al. 2017; Annuar et al. 2020).

Multi-wavelength extragalactic surveys generally follow a “wedding cake” strategy (e.g., Khedekar et al. 2010; Grogin et al. 2011), consisting of observations that are either shallow and wide, or deep and narrow. With finite telescope resources, the choice is to either focus on a small area with a long exposure time or cover a wider field at a shallower depth. Combining the two is maximally efficient: deep fields probe higher redshifts, whereas shallower all-sky surveys can probe larger volumes and are thus sensitive to the rarer, high-luminosity sources. For example, rare high-luminosity AGN are typically found in wide-area surveys, such as Stripe 82X, the X-ray augmentation of the SDSS Stripe 82 region with Chandra and XMM-Newton (LaMassa et al. 2013a,b; Peca et al. 2023; LaMassa et al. 2024). The eROSITA Final Equatorial Depth Survey (Brunner et al. 2022; Liu et al. 2022) is a very wide (~ 140 square degrees), but relatively shallow (~ 1.2 ks after accounting for vignetting effects), survey that has detected over 22,000 AGN at $z \lesssim 3$ and relatively high luminosities (Nandra et al. 2024). Meanwhile, some of the most sensitive pencil-beam observations are those performed with Chandra: the Chandra COSMOS-Legacy Survey (CCLS; Civano et al. 2016), and the Chandra Deep Fields North (CDF-N; Hornschemeier et al. 2000) and South (CDF-S; Giacconi et al. 2001). However, in all these surveys, the majority of the detected objects

are close to the detection limit and have relatively few counts.

One of the advantages of observing high-redshift AGN is that the K-correction shifts the X-ray spectrum to probe higher energies, and hence observations by, e.g., Chandra are somewhat less affected by obscuration (e.g., Brandt & Hasinger 2005; Hickox & Alexander 2018). However, simulations (Koss et al. 2015) have shown that a nearby CT AGN, NGC 3393, would have accurate measurements of its intrinsic luminosity only for $z < 0.2$, while an unobscured AGN with similar luminosity could be measured up to $z \approx 5$ with Chandra. As we show below, traditional obscuration indicators are unreliable for low-count X-ray spectra due to the degeneracies with sources at lower column densities (Koss et al. 2016). Furthermore, to match the intrinsic energy range of telescopes such as Swift/BAT (14–195 keV) or NuSTAR (3–79 keV), sources would need to be at $z \geq 5$, while the CCLS and CDF-S, which represent the deepest X-ray AGN surveys to date over their respective areas, have median redshifts of only $z \sim 1.28$ (see online catalog from Marchesi et al. 2016a) and $z \sim 1.03$ (see Table 1 of Tozzi et al. 2006), respectively. See Appendix A for a discussion the effective areas of Swift/BAT and other missions as a function of redshift.

Thus, two critical questions arise regarding deep AGN surveys below 10 keV, which we aim to address in this paper: (1) What fraction of distant AGN does Chandra miss due to obscuration? (2) How effectively do we recover the intrinsic spectral properties of those AGN (obscured and unobscured) that are identified? To explore these questions, we used the Swift/BAT AGN Spectroscopic Survey (BASS; Koss et al. 2017).

The Swift/BAT instrument has surveyed the entire sky in ultra-hard X-rays (14–195 keV; Barthelmy et al. 2005) detecting mainly nearby AGN with X-ray luminosities between 10^{41} and 10^{45} erg s⁻¹ (Baumgartner et al. 2013; Oh et al. 2018). BASS is a follow-up survey that has measured the emission lines (Koss et al. 2022b; Oh et al. 2022; Mejía-Restrepo et al. 2022), X-ray properties (Ricci et al. 2015, 2017c) as well as the IR and radio properties (Smith et al. 2020; Pfeifle et al. 2022; den Brok et al. 2022; Kawamuro et al. 2022; Bierschenk et al. 2024) of these AGN, which have luminosities similar to those in the Chandra and XMM deep surveys (Koss et al. 2022a). Koss et al. (2016) demonstrate that BASS is the least biased X-ray survey in terms of obscuration, with simulations showing that the Swift/BAT count rate is not affected by obscuring column densities up to 10^{23} cm⁻². Therefore, BASS AGN represent ideal templates which can be matched in luminosity to simulate AGN at higher redshifts. These well-understood

simulated spectra can then be used to quantify the selection effects in deep surveys (Koss et al. 2022a).

This paper focuses on the CCLS field, which has the largest contiguous survey area among deep-field programs (>100 ks effective exposure) with X-ray coverage. The COSMOS field (Cosmic Evolution Survey; Scoville et al. 2007) covers a 2 square-degree equatorial patch of the sky and consists of broadband observations from radio to X-rays. The Chandra-COSMOS survey (Elvis et al. 2009; Civano et al. 2016) covers 1.5 square degrees at an effective exposure of ~ 160 ks. The BASS AGN luminosity function is particularly well-matched to that of CCLS. The deep multi-wavelength and X-ray coverage of the COSMOS field is currently being augmented with JWST observations through the COSMOS-Web program (Casey et al. 2023), making it of particular interest to understand how well the most sensitive IR and X-ray instruments can detect distant obscured AGN.

Marchesi et al. (2016b) (henceforth, M16) present the X-ray spectral analysis for 1855 CCLS sources with at least 30 counts, where they fit phenomenological models of increasing complexity, choosing those that optimize the fit statistic. Lanzuisi et al. (2018) further model 67 of these sources that were determined to have at least a 5% probability of being CT with the MYTorus model of Murphy & Yaqoob (2009) combined with Markov chain Monte Carlo parameter estimation techniques. By summing the posterior distribution of the line of sight column density of individual sources that were above 10^{24} cm⁻², and accounting for identification and classification bias, the authors find 41.9 “effective” CT AGN in the sample.

This paper focuses on quantifying selection effects due to obscuration in CCLS. To fully address the question of how well we can recover intrinsic properties from Chandra observations, every study from every Chandra survey field would ideally be addressed. Indeed, the techniques used can be extended to other deep X-ray surveys (e.g., XMM-XXL, Menzel et al. 2016; the NuSTAR extragalactic survey, Alexander et al. 2013; CDF-S), as well as current and future missions (e.g., eROSITA, Predehl et al. 2021; NewAthena, Nandra et al. 2013, Cruise et al. 2024; AXIS, Reynolds et al. 2023; HEX-P, Madsen et al. 2024). We begin to address these questions in this paper by focusing on the CCLS, which is a reasonable starting point given its intermediate depth relative to other surveys.

Section 2 describes the template spectra and the simulated data set, and Section 3 presents our data analysis and results. We discuss the results in Section 4 and conclude in Section 5. Throughout the paper, we adopt

a cosmology of $H_0 = 71 \text{ km s}^{-1} \text{ Mpc}^{-1}$, $\Omega_m = 0.3$, and $\Omega_\Lambda = 0.7$, the same as that used in the CCLS X-ray study of M16. To make notation less cumbersome, we use $\log N_H$ as shorthand for $\log(N_H/\text{cm}^{-2})$, the log of the obscuring column density along the line of sight in units of cm^{-2} , and $\log L_{2-10,\text{int}}$ as shorthand for $\log(L_{2-10,\text{int}}/\text{erg s}^{-1})$, the log of the intrinsic 2–10 keV luminosity in units of erg s^{-1} .

2. SAMPLE AND SIMULATION OVERVIEW

2.1. *Swift*/BAT instrument and BASS

The BAT 70-month AGN sample reaches depths of at least $1.34 \times 10^{-11} \text{ erg s}^{-1} \text{ cm}^{-2}$ over 90% of the sky (Baumgartner et al. 2013) and comprises 858 nearby ($z \lesssim 0.3$ for unbeamed non-blazar) AGN (Koss et al. 2022c). Ricci et al. (2017c, henceforth, R17) present and characterize their broadband X-ray spectra using complementary soft X-ray observations by XMM-Newton, Swift/XRT, ASCA, Chandra, and Suzaku. Some of the properties they constrain are the intrinsic X-ray luminosity (in the 2–10, 20–50, and 14–150 keV bands), the intrinsic N_H , the slope of the X-ray power law continuum (Γ), and the temperature of the thermal plasma for obscured sources. The phenomenological models used are broadly classified into four groups: unobscured (352), obscured (386), blazars (97), and other non-AGN models (2). The 75 sources that were found to be CT using a phenomenological model were refit in XSPEC with the BNTorus model (Brightman & Nandra 2011) to better constrain their N_H values.

2.2. Source selection and simulations

Koss et al. (2017) and Koss et al. (2022a) note that the unbeamed BAT AGN span the moderate-to-high end of the X-ray luminosity function, rendering them appropriate analogs to the AGN detected at high redshifts in deep surveys. Indeed, the median intrinsic X-ray luminosity of the non-blazar BASS sample is $L_{2-10,\text{int}} = 10^{43.41} \text{ erg s}^{-1}$, compared to $10^{43.69} \text{ erg s}^{-1}$ for the 2291 CCLS sources with intrinsic 2–10 keV luminosities well-constrained from the redshifts of the optical and IR counterparts (Marchesi et al. 2016a). For this study, we focus on this subset of the CCLS sample (CCLS*) to characterize its observational biases regarding obscuration. Fig. 1 shows how the redshift-luminosity distribution of BASS non-blazar AGN compares with that of the CCLS*. Note that the luminosity distributions are very similar despite the BASS AGN being in the local universe because the BASS survey covers the full sky. However, since it is a flux-limited survey, there are few BASS AGN with X-ray luminosities below $10^{42} \text{ erg s}^{-1}$.

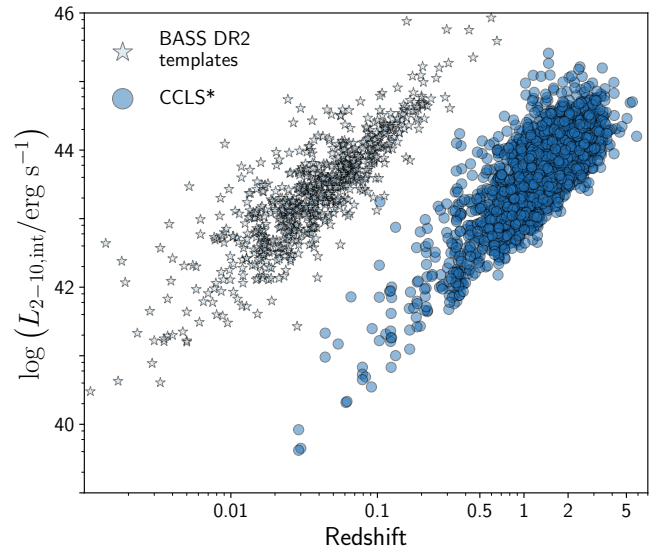


Figure 1. Intrinsic 2–10 keV X-ray luminosity versus redshift for BASS and CCLS sources. Distribution of the rest-frame hard X-ray luminosity versus redshift of non-blazar BASS AGN (stars) and CCLS* (dots). Note that Swift/BAT-selected AGN cover a range of X-ray luminosities similar to that of CCLS*.

To generate our data set, we first took models from R17 for sources that were either unobscured or obscured, excluding beamed AGN and non-AGN sources. This resulted in 738 AGN models. We further selected models for sources with spectroscopic redshift measurements from optical counterparts and excluded five models of anomalous sources (i.e., sources with significant pileup components, contamination from the Perseus cluster, and/or with inconsistencies in the X-ray model). This resulted in 698 AGN X-ray models from the BASS catalog, which we use as templates to simulate the CCLS* field. These models were constructed using high-quality broadband spectra from nearby ultra-hard X-ray-selected AGN sampled from the entire sky; the median number of soft X-ray counts is 1525.5. See Appendix B for a brief overview of the R17 models.

To select a subset of BASS AGN models with a luminosity and redshift distribution well-matched to CCLS*, we adopted the intrinsic luminosity distribution of AGN in the CCLS* from Marchesi et al. (2016a), where they convert from the observed luminosities assuming an X-ray spectral index of 1.8. Note that we did not attempt to match the CCLS* N_H distribution. See Appendix C for further discussion. We then modeled the CCLS* intrinsic X-ray luminosity function as a probability distribution function (pdf) using kernel density estimation. We drew random values from the estimated luminosity pdf, and selected template models with the closest

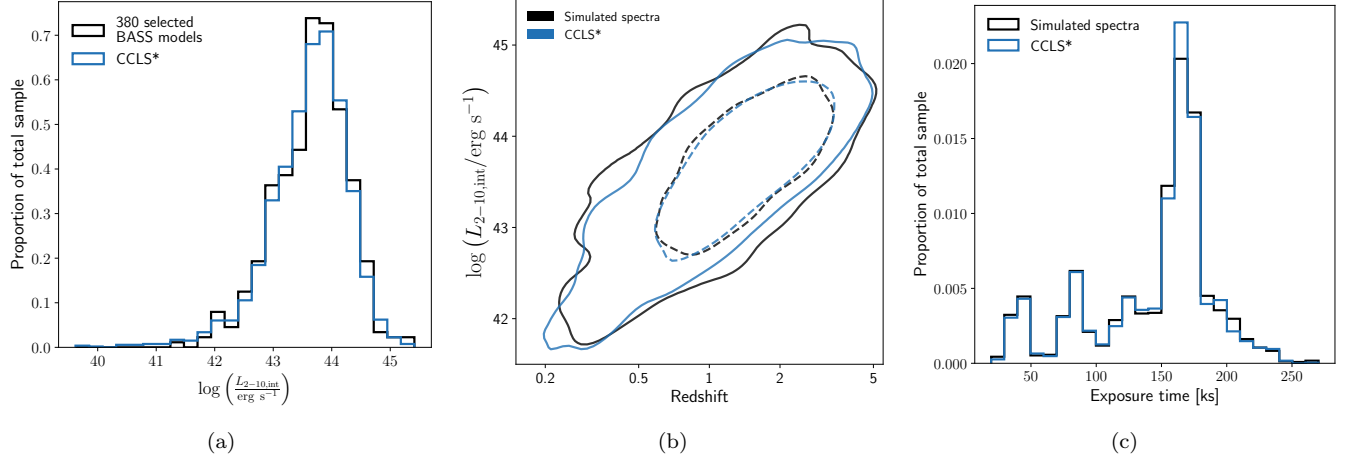


Figure 2. (a) **Luminosity matching.** The intrinsic X-ray luminosity distributions of the CCLS* catalog (blue) and the selected template models (black). (b) **Redshift matching.** Comparison of the CCLS* catalog (blue) and the simulated data set (black) in luminosity-redshift space. 95% of the sources lie within the solid curves and 68% of the sources lie within the dashed curves. (c) **Exposure time matching.** Distribution of the exposure times for the 2280 simulations (black) compared with that of the 2291 spectra in CCLS* (blue).

$L_{2-10,\text{int}}$ (in log space), without allowing template models to be selected twice. We found that selecting 380 template models allowed us to maximize the number of different AGN models used while reasonably matching the CCLS* luminosity distribution. See Fig. 2(a).

In order to have a similar number of sources in our simulated dataset as in CCLS*, each of the 380 selected template models was used to simulate AGN spectra at six redshifts, resulting in a data set of 2280 simulated spectra. The redshift values for each simulation were chosen based on $L_{2-10,\text{int}}$ as follows: A pdf of redshift was calculated for each of twelve $\log L_{2-10,\text{int}}$ bins using kernel density estimation from the CCLS* sources. Then, for each BASS model, six random redshift values were drawn from the estimated pdf of its luminosity bin. The resulting luminosity-redshift distribution is shown together with that of CCLS* in Fig. 2(b).

Finally, we assigned an exposure time to each simulation by drawing random samples from a pdf defined by the exposure time distribution of CCLS*. The median exposure time of the simulated data set is 161.4 ks, while that of the CCLS* sample is 162.2 ks. See Fig. 2(c). The full list of selected BASS models and their assigned redshifts and exposure times is presented in Table 4.

To simulate Chandra spectra in the CCLS field, each selected BASS model was imported into XSPEC (v12.11; Arnaud 1996) and modified as follows:

1. The column density parameter of any component representing Galactic absorption (`phabs.nH` or `TBabs.nH`, depending on the R17 model) was changed to $N_{\text{H,gal}} = 2.5 \times 10^{20} \text{ cm}^{-2}$ to place the

AGN behind the same Galactic line-of-sight as the CCLS field (Kalberla et al. 2005).

2. The redshift parameter (`z` or `Redshift`) of each relevant model component was changed to the assigned simulated redshift value.
3. The `norm` parameter of each relevant model component was rescaled so that the flux changed according to the new luminosity distance, while the intrinsic properties of the simulated source remained unchanged. To do this, we calculated $L'_{2-10,\text{int}}$, the intrinsic 2–10 keV luminosity using the new redshift value with the original `norm` values, and then multiplied the `norm` parameters by $L_{2-10,\text{int}}/L'_{2-10,\text{int}}$.

The `fakeit` command was then used to simulate the spectra through the Chandra response, introducing only Poisson noise in the procedure. We used Chandra-ACIS on-axis response files from cycle 14 (near when most COSMOS data were collected), and exposure times were assigned as described above. Note that the effective exposure times account for off-axis positions of the Chandra observations (see Civano et al. 2016). See Appendix D for a discussion of potential selection effects generated by the `fakeit` procedure.

2.3. Illustrative examples

To demonstrate the effect of obscuration on the quality of Chandra observations, we selected three pairs of BASS models, with $\log L_{2-10,\text{int}} = 43.15$, 43.71, and 44.20. These represent the approximate first, second, and third quartiles of the intrinsic X-ray luminosity

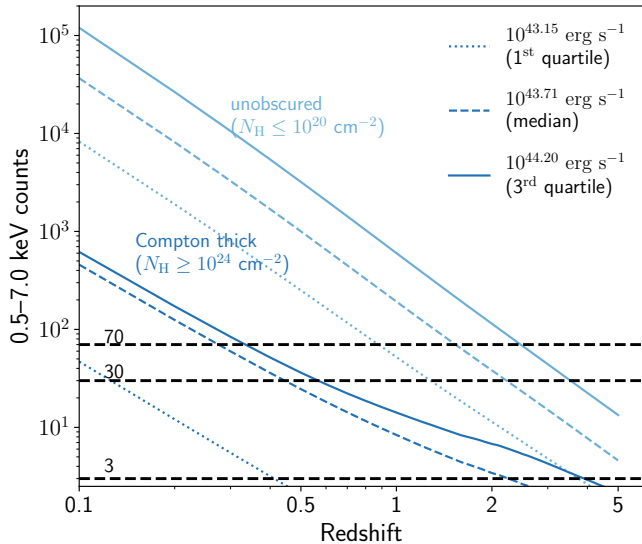


Figure 3. Demonstration of the importance of obscuration on the detection and count fraction as a function of redshift using nearby BAT AGN. We compare three pairs of BASS models, each with an unobscured model (light blue) and a CT model (dark blue). The three pairs are at $\log L_{2-10, \text{int}} = 43.15$ (dotted), 43.71 (dashed), and 44.20 (solid), which correspond to the first, second, and third quartiles of the CCLS* luminosity distribution. Horizontal cutoffs are shown at three counts (the faintest possible detection), 30 counts (spectral modeling with at least one free parameter), and 70 counts (spectral modeling with at least two free parameters). Although the median luminosity unobscured source still has 30 counts up to $z \sim 2$, its CT counterpart cannot be reliably detected beyond that redshift. Among CT simulations, uneven vertical spacing is due to variation in the exact N_{H} values, which are $10^{24.79} \text{ cm}^{-2}$ (1st quartile luminosity), $10^{24.07} \text{ cm}^{-2}$ (median luminosity), and $10^{24.11} \text{ cm}^{-2}$ (3rd quartile luminosity). The bump in the signal of the high-luminosity CT source at $z \sim 1.5$ is due to photons from the reflected component beginning to enter the Chandra band pass.

distribution of CCLS* (and of our 380 selected template spectra). Each pair consists of a completely unobscured model ($N_{\text{H}} \leq 10^{20} \text{ cm}^{-2}$) and a CT model ($N_{\text{H}} \geq 10^{24} \text{ cm}^{-2}$). We recorded the net 0.5–7.0 keV Chandra counts as a function of redshift for each model using an exposure time of 162 ks, the median exposure time for the CCLS sample. To reduce the effects of Poisson noise, we took the mean of 10^6 simulations at each redshift. The results are shown in Fig. 3. Note that while the median luminosity unobscured model has more than 30 counts at $z \sim 2$, its CT counterpart cannot be reliably detected, and even the highest luminosity CT source has fewer than 30 counts for $z \gtrsim 0.5$. Also note that high-luminosity CT AGN exhibit a relative increase in data quality for $z \gtrsim 1.5$, because photons with

intrinsic energies less affected by obscuration begin to be detected by Chandra due to redshifting of the spectra. The BASS IDs used here are 643, 325, and 456 for the CT models and 774, 328, and 771 for the unobscured models.¹

3. DATA ANALYSIS AND RESULTS

3.1. Detection and counts

To measure the counts of each simulated spectrum, the simulated spectra were imported into XSPEC, and only channels in the 0.5–7.0 keV range were noticed, following the approach of M16. Accurately reproducing the Chandra background given the array of off-axis angles and overlapping fields was difficult and the effect is small (there are < 2 expected background counts for an on-axis source in the CCLS data; Civano et al. 2016), so as an approximate approach we did not include a background in our fits. This means our study conservatively overestimates the ability to model source spectra (which was only done for sources with at least 30 counts). See Appendix D for further discussion of the background and minimum detection threshold.

First, any spectrum with fewer than three counts (the minimum in CCLS*) was set to zero counts. Thus, three counts is considered a Chandra “detection.”² For the detection study below 30 counts, we had an excess of spectra with few (< 10) counts. To correct this, we included a function to randomly reduce the number of sources at the same rate that Chandra would not detect because of background.³ With this approach, the detection rate for our simulated sample was 1532/2280 (67.2%). Fig. 4(a) shows the resulting count distribution for the 1532 detected simulated spectra compared with that of the CCLS* sample.

Our counts distribution matches well for sources with more than ~ 200 counts. These are bright sources with high signal-to-noise ratios, for which background is negligible. Compared with CCLS*, we are missing sources below ~ 100 counts. This is likely because our template models are drawn from local Swift/BAT-selected AGN, in which obscured and CT sources are more likely to be detected because of their higher energy coverage relative to deep surveys like CCLS (see Fig. 13 in Appendix C). In Fig. 4(b), it is shown that obscured and CT simulations are skewed to lower counts relative to

¹ See bass-survey.com/dr2.html for complete catalog information on these sources, including source and counterpart identifiers.

² We chose to set the threshold in counts instead of flux since that grounds our study in detector space.

³ The CCLS notes that there is significant incompleteness below 20 counts (Civano et al. 2016).

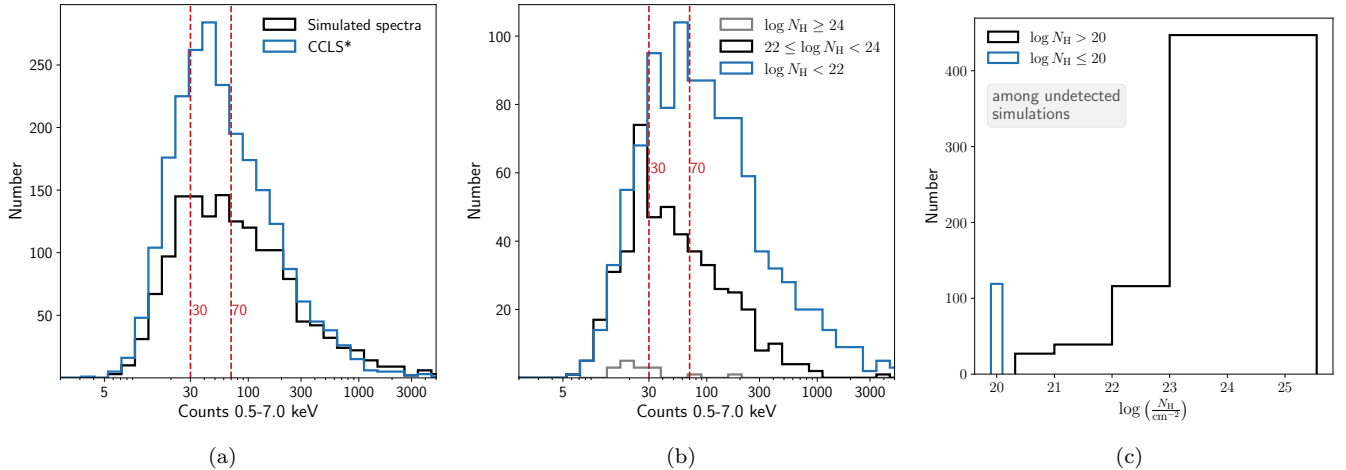


Figure 4. Net counts of simulated spectra. (a) Comparison with CCLS*. The Chandra counts in the 0.5–7.0 keV band of the 1532 simulated spectra considered detected (black; see text), compared with that of the 2291 CCLS* spectra (blue). **(b) Obscured and unobscured detected spectra.** Obscured simulations (black) lean more toward the low-count regime than do their unobscured counterparts (blue), and 10/17 CT simulations (gray) have fewer than 30 counts. **(c) N_H distribution of sources undetected in simulations.** Undetected sources with zero counts (748) are largely heavily obscured and CT models. The spike at $\log N_H = 20$ (shown separately in blue) is due to the application of the selection function below 30 counts and the fact that completely unobscured sources make up a significant portion of our simulations.

all other simulations, which is a well known effect (e.g., Brandt et al. 2000). Fig. 4(c) further shows that heavily obscured sources comprise a significant portion of undetected sources. There is a spike at $\log N_H = 20$ (shown separately in blue) due to the application of the selection function below 30 counts, and the fact that entirely unobscured sources make up a significant portion of our simulations. Note that all models with $\log N_H \leq 20$ are labeled as $\log N_H = 20$ in the BASS survey since Galactic N_H dominates below that point, and therefore the intrinsic column density cannot be reliably constrained.

Table 1 summarizes the number of simulations detected. Fig. 5 presents the percentages of spectra with ≥ 30 and ≥ 70 counts, in bins of luminosity and obscuration column density. *In particular, only 5/192 (2.60%) of CT simulated spectra were detected with at least 30 counts*, the minimum threshold for spectral modeling that we adopted from M16. This means that only five of the fitted spectra were simulated with CT models because of the inherently low counts in the simulation. Note that the Poisson fluctuations introduced by `fakeit` also affect the counts distribution, so the detection fraction of obscured sources can be considered an upper bound, since the non-detections due to noise would only make the fraction lower.

3.2. Fitting procedure

Next, we investigate how well Chandra can recover the parameters of the sources that we detect. To do so, we follow the CCLS fitting procedure outlined in Sec. 4.1

Table 1. Number of simulations detected, and those with at least 30 and 70 counts. Percentages of the total in each row are shown in parentheses.

	Total	Detected	30+	70+
All sims	2280	1532	1179	751
		(67.2%)	(51.7%)	(32.9%)
Obscured	1056	493	316	171
($\log N_H \geq 22$)		(46.7%)	(29.9%)	(16.2%)
CT	192	17	5	2
($\log N_H \geq 24$)		(8.9%)	(2.6%)	(1.0%)

of M16 for all CCLS sources with at least 30 counts. They adopted a four-step fitting procedure, which we summarize here. In each step, the quality of the fit was measured with the C statistic (C ; Cash 1979),⁴ which is particularly useful for data sets with low counts per bin, where Gaussian assumptions break down. Since we did not include background spectra in the simulations, we can use the C statistic, which assumes only Poisson noise. For each subsequent fit, the criterion for improvement over the previous fit was $\Delta C \equiv C_{\text{old}} - C_{\text{new}} > 2.71$. We used the `XSPEC error` command to calculate 90%

⁴ $C = 2 \sum_i \left(m_i - n_i + n_i \ln \left(\frac{n_i}{m_i} \right) \right)$, where n_i (m_i) is the observed (predicted) counts in bin i .

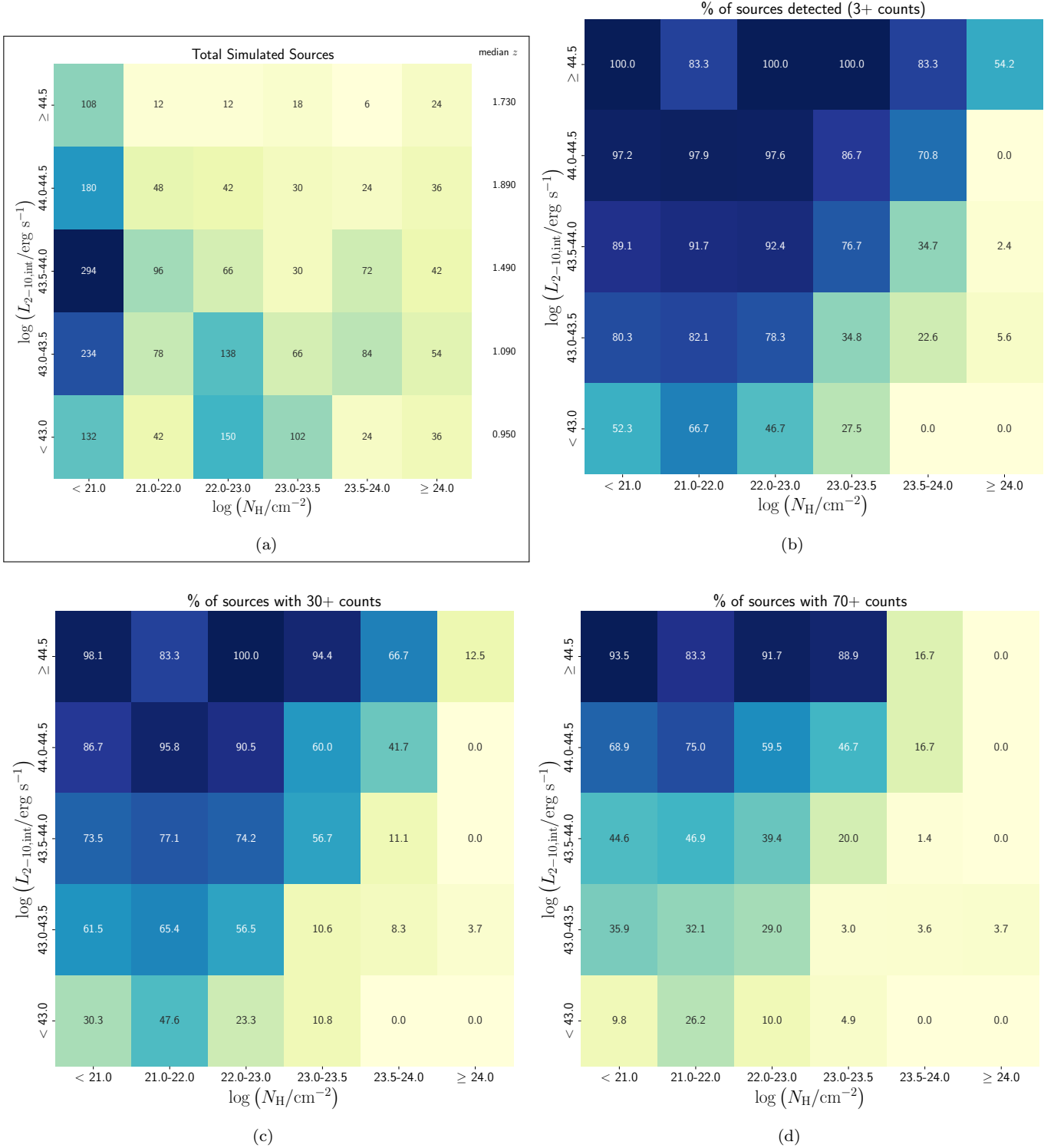


Figure 5. Chandra detection fractions of the simulated dataset organized in bins of intrinsic X-ray luminosity (vertical) and obscuring column density (horizontal). Dark blue indicates high fractions and pale yellow indicates low fractions. **(a)** Total number of simulated sources and the median redshift of each luminosity bin. The expected positive correlation between redshift and luminosity is illustrated in Fig. 2(b). **(b)–(d)** Percentage of simulations with at least 3, 30, and 70 counts. The percent values are displayed in each square. Simulated spectra with ≥ 30 counts sources were fit with at least one free parameter, and those with ≥ 70 counts were fit with at least two free parameters.

confidence intervals. All spectra were grouped to at least three counts per bin for fitting. In what follows, $N_{\text{H,gal}}$ was set to $2.5 \times 10^{20} \text{ cm}^{-2}$, and all redshifts were fixed to the values used in the simulation model.

1. If the spectrum had fewer than 70 counts, we fit to an absorbed power law ‘`phabs*(zphabs*zpow)`’ with Γ fixed to 1.9. Only `zphabs.nH` (N_{H}) and `zpowerlw.norm` were free to vary.
2. For all sources with at least 30 counts, we then fit the spectrum to the same absorbed power law model as in step 1, but with `zpowerlw.PhoIndex` (Γ) also free to vary.
3. For all sources with at least 30 counts, we then added an additional unabsorbed power law with $\Gamma_2 = \Gamma_1$: ‘`phabs*(zphabs*zpow + const*zpow)`’. This represents intrinsic emission that escapes through sight lines of column density lower than that of the dense circumnuclear obscurer and is subsequently scattered into the direction of the detector. The relative normalization of the secondary power law (`constant.factor`) is a consequence of both the covering factor of the torus and the viewing angle (McKaig et al. 2023), and as noted in previous studies (e.g., M16, R17, Peca et al. 2023), it should not exceed a few percent of the primary component (see discussion in Appendix F). Consistent with M16, `constant.factor` was constrained to be < 0.15 (private correspondence).⁵
4. For all sources with at least 30 counts, we added a Gaussian component to whatever the best-fit model was at this stage to represent the iron $K\alpha$ line. `zgauss.LineE` was fixed to 6.4 and `zgauss.Sigma` was fixed to 0.1.

A summary of how many simulated spectra settled on each fit is presented in Table 2. The goodness-of-fit statistics are discussed in Appendix E and the full catalog of the simulation fits is presented in Table 5. Since the BASS catalog reports all best-fit N_{H} values $\leq 10^{20} \text{ cm}^{-2}$ as 10^{20} cm^{-2} , after fitting, we imposed the same lower limit on all of our best fit N_{H} values and their lower limits for easy comparison with the BASS models. These fits were considered to be consistent with a column density of zero. Among the 1179 best fits, 906

⁵ We also set a lower limit of 0.001 (Gupta et al. 2021), in order to not over-index on data points at the highest energies of the Chandra band pass, which would have the most significant background. Any fits that hit the upper or lower limits were discarded.

Table 2. Summary of fitting results. Fit numbers correspond to steps 1–4 described in Sec. 3.2. Percentages of the total in each row are shown in parentheses. Entries with “—” indicate that the column is not applicable by definition of the fit. Entries with “by def” underneath them are always true by definition of the fit.

Fit	Total	< 70 cts	Γ free	2PL	Fe line
1	355	355 (by def)	—	—	—
2	711	50 (7.0%)	711 (by def)	—	—
3	57	17 (29.8%)	49 (86.0%)	57 (by def)	—
4	56	6 (10.7%)	52 (92.9%)	3 (5.4%)	56 (by def)
ALL	1179	411	812	60	56
FITTED		(34.9%)	(68.9%)	(5.1%)	(4.8%)

had N_{H} values consistent with zero with 90% confidence, among which 117 had completely unconstrained N_{H} (all possible values fell within the 90% confidence intervals). Meanwhile, among simulations with at least 30 counts, 529 were simulated with $\log N_{\text{H,sim}} \leq 20$.

3.3. Parameter recovery: photon index

To quantify how well parameters were recovered, we focused on the photon index Γ and the absorption column density N_{H} . For Γ , we compute the error $\Delta\Gamma = \Gamma_{\text{meas}} - \Gamma_{\text{sim}}$. The histograms of the results are shown in Fig. 6(a). $\Delta\Gamma$ is peaked around zero, with a median value of +0.03, and 68% of sources within the interval $[-0.29, 0.36]$. With a Spearman’s correlation coefficient of ($r_{\text{S}}(1177) = 0.076, p = 0.009$), a mildly significant correlation was found between $|\Delta\Gamma|$ and z_{sim} , indicating that the photon index is less accurately measured for sources at higher redshift. There was a significant negative correlation between $|\Delta\Gamma|$ and net counts ($r_{\text{S}}(1177) = -0.240, p < 10^{-16}$),⁶ which is expected, since higher quality data should have less error in the measured slope. There was a negative correlation between $\Delta\Gamma$ and Γ_{sim} , ($r_{\text{P}}(1177) = -0.249, p < 10^{-5}$),

⁶ We used the Spearman’s correlation coefficient (r_{S}), which is based on ranks of the data rather than the actual values, because the absolute error, net counts, and $\log N_{\text{H}}$ are not normally distributed. We used Pearson’s coefficient (r_{P}) when measuring the relationship between $\Delta\Gamma$ and Γ_{sim} (in any case, the Spearman’s coefficient also indicates a correlation between those two variables).

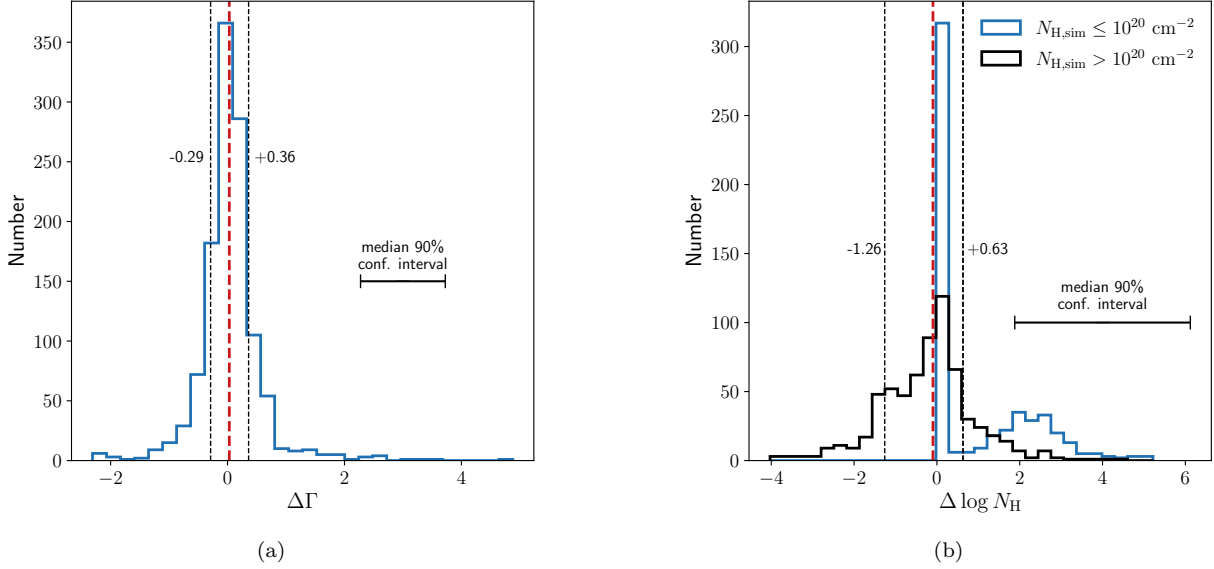


Figure 6. Error histograms. For each of Γ and $\log N_{\text{H}}$, we calculate the error of the measured value relative to the simulated value. **(a) Accuracy of measured Γ .** The vertical red dashed line indicates the median $\Delta\Gamma$ at $+0.03$. 68% of the spectra lie between the black dashed lines at -0.29 and $+0.36$. The error bar indicates the median size of the 90% confidence interval computed by XSPEC, which is 0.73 . **(b) Accuracy of best-fit N_{H} (log scale).** For simulations with some obscuration (black), the distribution is peaked around zero with a median of -0.10 dex (indicated by the dashed red line) and 68% of spectra lying between the dashed black lines at -1.26 dex and $+0.63$ dex. In contrast, there is a tail of significantly overestimated spectra for simulations with an intrinsic N_{H} consistent with zero (blue). The error bar indicates the median size of the 90% confidence interval computed by XSPEC (among those that were finite), which is 2.12 dex.

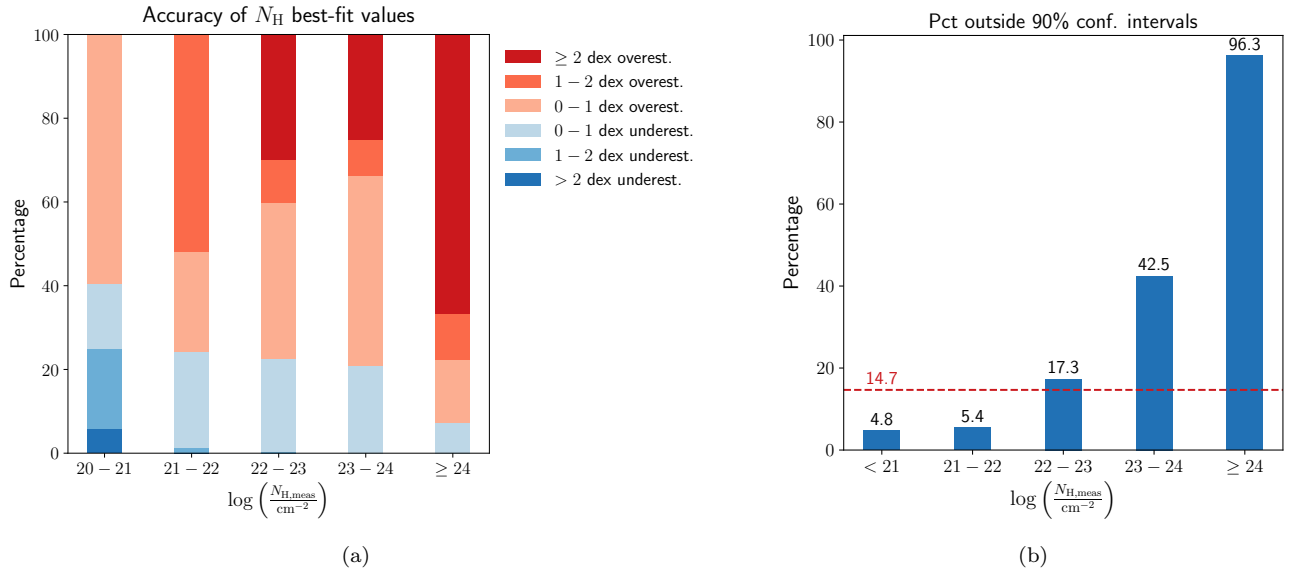


Figure 7. CT overestimation. We investigate the accuracy of the best-fit N_{H} estimations and the 90% confidence intervals. **(a) Accuracy of best-fit N_{H} measurements.** In bins of best-fit measured N_{H} , we show the proportion of fits that are accurate to different dex values. Among the 27 spectra that infer CT space ($\log N_{\text{H,meas}} \geq 24$), 21 (77.8%) are overestimated by > 1 dex. **(b) The proportion of N_{H} fits that are inaccurate within 90% confidence intervals.** The percentage of fitted spectra in each N_{H} bin whose N_{H} was incorrectly determined with 90% confidence. The red dashed line indicates the percentage for the entire fitted dataset.

indicating that softer (harder) slopes tend to be overestimated (underestimated). Additionally, a mild correlation was found between (signed) $\Delta\Gamma$ and $\log N_{\text{H},\text{sim}}$ ($r_{\text{S}}(1177) = 0.0659, p = 0.024$). Among the fits with Γ as a free parameter, 69.21% (562/812) were accurate within the 90% confidence intervals calculated by XSPEC. Among those that were outside of the 90% confidence intervals, 40.00% (100/250) were underestimated and 60.00% (150/250) were overestimated.

3.4. Parameter recovery: column density

Similarly, we computed $\Delta \log N_{\text{H}} = \log N_{\text{H},\text{meas}} - \log N_{\text{H},\text{sim}}$. Note that this error is in logarithmic space. The results are shown in Fig. 6(b). There was a positive correlation between $\Delta\Gamma$ and $\Delta \log N_{\text{H}}$ ($r_{\text{S}} = 0.358, p < 10^{-4}$), indicating that underestimated Γ values tend to be paired with underestimated obscuration values. Furthermore, among the 250 fits (with Γ free to vary) for which Γ_{sim} did not lie within the 90% confidence intervals of Γ_{meas} , 67 of them (26.8%) measured N_{H} outside of the 90% confidence intervals. Meanwhile, among the 562 fits that measured Γ correctly within the 90% confidence intervals, 36 of them (6.4%) measured N_{H} outside the 90% confidence intervals. In all but two cases, when Γ was below the 90% confidence interval (i.e., the slope was estimated to be too soft), N_{H} values were also underestimated. These correlations are the result of a degeneracy in power-law fits to AGN X-ray spectra, which is further discussed in Sec. 4.2.

The error in the best-fit $\log N_{\text{H}}$ shows a clear excess of overestimated sources. The overestimation of N_{H} in X-ray surveys is a well-known issue (e.g., Appendix A of Akylas et al. 2006) and is taken into account in several X-ray population studies (e.g., Simmonds et al. 2018; Peca et al. 2021, 2023), and in this study we quantify the effect for a large sample for the first time.

Furthermore, we know that only five CT simulations were detected with at least 30 counts—only 0.42% of the 1179 total that were fitted. Meanwhile, 472 spectra (40.03% of fitted sources) had best-fit $\log N_{\text{H},\text{meas}} \geq 22$, and 993 (84.22%) were obscured within 90% confidence intervals. Among those, 27 (2.29%) had best-fit $\log N_{\text{H},\text{meas}} \geq 24$, and 158 (13.40%) were CT candidates within 90% confidence intervals. Thus, many of these column densities were overestimated.

Interestingly, the error in the best-fit N_{H} is centered about approximately zero (median of -0.10 dex, while the median 90% confidence interval is 2.12 dex wide) for all spectra with $\log N_{\text{H},\text{sim}} > 20$ (although the distribution is broad, with 68% of fits in the interval $[-1.26, 0.63]$). The excess of significantly overestimated column densities arises predominantly from simulations

of completely unobscured models ($\log N_{\text{H},\text{sim}} \leq 20$, consistent with zero). A spike in zero-error N_{H} values can also be seen for the $\log N_{\text{H},\text{sim}} \leq 20$ sample. This is due to the lower limit imposed at $\log N_{\text{H}} = 20$.

Fig. 7(a) shows the distribution of errors in best-fit N_{H} . While most spectra with $\log N_{\text{H},\text{meas}} \leq 21$ are within one dex of the simulated value, the proportion of significantly overestimated increases in each subsequent bin. Among the spectra measured to be CT, 66.6% (18/27) are actually unobscured sources ($\log N_{\text{H}} \leq 22$) whose column density is overestimated by at least two dex, suggesting that X-ray measurements of low signal to noise AGN with fitted values indicating high obscuration are unreliable.

Conversely, among the five CT spectra detected with at least 30 counts, two were measured to be CT, one was measured to be obscured, and two were measured to have N_{H} consistent with zero with upper limits on $\log N_{\text{H}}$ less than 24.

If instead of the best-fit N_{H} , we look at the 90% confidence intervals, we find that the N_{H} for nearly all highly obscured and CT sources are inaccurate. While the measured N_{H} is accurate for 95.0% of simulations of unobscured AGN ($\log N_{\text{H}} < 22$), only 70.8% of those measured as obscured, and 3.7% of those estimated to be CT, are accurate within the error bars. See Fig. 7(b). No similar patterns were found among the net counts or z_{sim} distributions.

3.5. False CT sources

To investigate the phenomenon of overestimated column densities, we restrict our attention to the 11 spectra that had $\log N_{\text{H},\text{sim}} \leq 20$ and $\log N_{\text{H},\text{meas}} \geq 24$ (the “false CT sources”). We note that none of the false CT sources had 90% confidence intervals that extended below $\log N_{\text{H}} = 23.5$. Moreover, the false CT sources were not necessarily those with few counts: 4/11 had counts above 100, the median of the 1179 fitted simulations.

All of these fits settled on a double power law (2PL) fit (step 3 described in Sec. 3.2). 4/11 had a fixed photon index and none included an iron $\text{K}\alpha$ line. Fig. 8 shows their secondary normalizations versus net counts, compared with the other 2PL fits in our simulated sample as well as those of M16. It is notable that almost all of our fits that settled on a secondary normalization very near the upper limit turned out to be false CT source. Among the 145 fits that had N_{H} overestimated by at least 2 dex, 21.4% fit to a 2PL, compared with 2.5% for the rest of the fits. Conversely, 51.6% of the 60 2PL fits overestimated N_{H} by at least 2 dex, compared with only 10.1% of all other fits. Fig. 19 in Appendix F shows a histogram of $\Delta \log N_{\text{H}}$ for these fits.

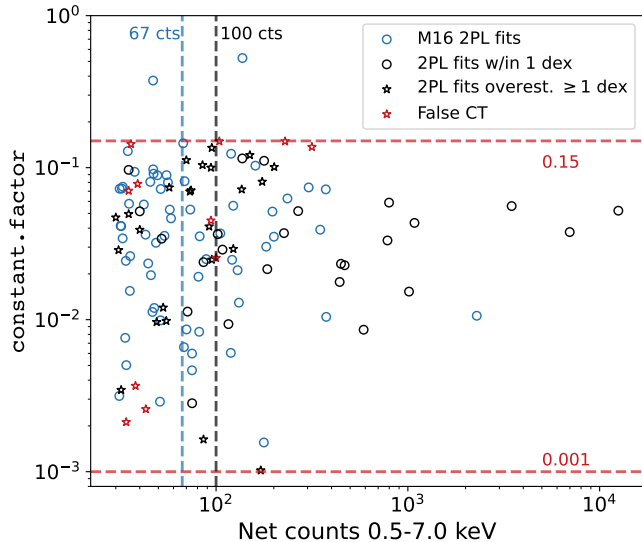


Figure 8. Properties of 2PL fits. For each of our 60 2PL fits, we show the relative normalization of the secondary power law versus the net counts in the 0.5–7.0 keV band. 2PL fits that measured N_{H} accurately to within 1 dex are shown in black circles, while those that were inaccurate by at least 1 dex are shown in black stars. Red stars represent the false CT fits, which had best-fit $\log N_{\text{H}} \geq 24$ and $N_{\text{H},\text{sim}} \leq 20$, and all of which settled on a 2PL fit. The 67 2PL fits of M16 are shown as blue circles for comparison. The red dashed lines indicate the upper and lower limits on the secondary normalization that we set during our fitting procedure, and the vertical dashed lines indicate the median counts of the full simulation sample (black; 100 cts) and the full sample of M16 (blue; 67 cts).

In general, for single power law fits, there is degeneracy between Γ and N_{H} since an unobscured softer power law can mimic the behavior of an obscured source and a harder continuum (perhaps with a reflected component). This explains the correlation reported in Sec. 3.4, wherein overestimates of Γ were correlated with overestimates in N_{H} . The photon index distribution of the false CT sources skews high relative to the simulation sample. To assess this, the Γ_{meas} of false CT sources were compared to the full simulation sample using a modified Z-score test⁷ with bootstrapped significance (10^5 samples). The false CT subset exhibited significantly higher Γ_{meas} values ($p = 0.0007$). This suggests that the necessity of a secondary power law is due to the sharper drop-off of the primary component.

We refit the 11 false CT spectra using the same procedure outlined in Sec. 3.2, but without step 3, so we did

⁷ $Z_{\text{mod}}(X_i) = (X_i - \text{median}(X))/\text{MAD}(X)$, with $\text{MAD}(X) = \text{median}|X_i - \text{median}(X)|$. We used the 95th percentile of the modified Z-score values as our test statistic.

not allow a 2PL fit. After doing so, 9/11 of the spectra were fitted to correct N_{H} values within 90% confidence intervals. Note that the Γ_{meas} shifted to lower values for these fits; using the same method as above, we found no significant difference between the Γ_{meas} values and those of the entire sample ($p = 0.05$), consistent with the fact that a 2PL with higher Γ_{meas} values is degenerate with a single, softer power law.

The 2/11 refits that still overestimated N_{H} were BASS ID 136 at $z_{\text{sim}} = 1.86$ and BASS ID 376 at $z_{\text{sim}} = 3.74$, each of which had fewer than 40 counts. Upon inspection, both seem to be a case of the $N_{\text{H}}-\Gamma$ degeneracy discussed above for single power law fits. The former fit to values of $\Gamma = 1.9$ (fixed) and $\log N_{\text{H}} \in [21.76, 23.27]$, while the BASS simulation model had $\Gamma = 1.72$ and $\log N_{\text{H}} = 20$. The latter fit to values of $\Gamma = 5.20$ and $\log N_{\text{H}} \in [23.68, 24.52]$, while the BASS simulation model had $\Gamma = 1.97$ and $\log N_{\text{H}} = 20$.

Examples of the false CT spectra and their refits are presented and discussed in detail in Appendix G.

3.6. Refitting with a torus model

As pointed out in Lanzuisi et al. (2018), phenomenological models are not optimized to correctly identify CT AGN since they do not take into account Compton scattering of photons nor the geometry of the obscuring torus. This is in addition to the $N_{\text{H}}-\Gamma$ degeneracy mentioned above. These considerations become especially important for $\log N_{\text{H}} \geq 23$ (e.g., Yaqoob 1997). Therefore, the phenomenological modeling of M16 is followed by a study of 67 of the sources with $\Gamma_{\text{meas}} \leq 1.4$ and $\log N_{\text{H},\text{meas}} \geq 23$, presented in Lanzuisi et al. (2018). These CT candidates were fit to the physically motivated MYTorus model (Murphy & Yaqoob 2009), and using a novel Monte-Carlo parameter estimation technique, 41.9 of the candidates were measured to be CT.

We used the MYTorus model implemented in Lanzuisi et al. (2018) to refit the 11 false CT sources. For simplicity, we use the XSPEC `error` command to calculate 90% confidence intervals on N_{H} instead of the more sophisticated approach used in that study. A detailed description of the model and its rationale can be found in Lanzuisi et al. (2018), which we briefly summarize here. The model included all three MYTorus components (the zeroth order continuum, the reprocessed continuum, and the fluorescent emission lines) as well as a secondary power law restricted to be $< 5\%$ of the normalization of the primary continuum (i.e., `phabs * (const * zpow + torusScat + torusLines + zpow * torusZeroCont)`). The inclination angle was fixed to 75° , the photon index was fixed to 1.8, the redshift was fixed to the value used for the

simulated spectrum, and all N_{H} parameters were tied to each other. This left three free parameters in the fit: N_{H} , the normalization of the primary power law, and the relative normalization of the secondary power law.

Zero of the 11 previously false CT sources were measured to be CT within 90% confidence intervals, and 10/11 were correctly measured to have N_{H} consistent with zero. Best-fit values can still be unreliable, as 6/11 spectra still had $\log N_{\text{meas}} > 20$, and one had $\log N_{\text{meas}} > 23$. This is expected since the physical torus models assume some degree of obscuration at the adopted fixed inclination angle. These results emphasize both the importance of refitting CT candidates to a physical torus model (e.g., MYTorus; BNtorus; borus, Baloković et al. 2018, 2019; and others), as well as using robust error estimators, such as Monte Carlo or Bayesian methods, to constrain N_{H} .

3.7. Parameter recovery: Fe line

163 of the 380 selected BASS models included a Gaussian component to represent the narrow Fe K α line and thus, 978 simulations included a Gaussian component. Among the simulated spectra with at least 30 counts, 371 included a Gaussian component, 23 of which were recovered. The remaining 33 fits that included a Gaussian component were not simulated with one, suggesting that those spectra were over-fit to spurious features.

4. DISCUSSION

4.1. Obscuration bias

Our results suggest that Chandra is inefficient at identifying obscured and CT AGN in the redshift range of 0.5–3.0. Only 493/1056 (17/192) simulated obscured (CT) sources were detected, and among those with at least 30 counts, 315/316 (3/5) were detected to be obscured (CT) within 90% error bars, out of 993 (150) total simulated spectra that were measured to be obscured (CT) with 90% confidence. Fig. 5 can be interpreted as a coarse-grained selection function to recover the intrinsic populations of AGN at different luminosities and column densities, based on the detected numbers (assuming the N_{H} and intrinsic luminosities are themselves accurately measured). This suggests that many sources currently classified as obscured and CT, especially those at low luminosity, probably have overestimated column densities. One potential cause of this overestimation is the misuse of the 2PL model, discussed below in Sec. 4.2 and Appendix F. While the N_{H} bias towards higher column densities has been well demonstrated on single sources (e.g., Marchesi et al. 2018; Tanimoto et al. 2022), our study represents the first time it is quantified in a large ($N > 100$) study of an entire AGN population.

The results in Fig. 7 highlight the danger of using best-fit values to characterize the survey data. Even the $22 \leq \log N_{\text{H}} < 23$ bin, which correctly measures the N_{H} to 90% confidence for 82.7% of sources, has best-fit values that are inaccurate by over 1 dex for nearly 40% of sources. The current approach of using best-fit values for a distribution that is highly biased, either due to the low count rates or limitations in fitting models, results in many derived values that are significantly outside their predicted errors. Due to its systematic nature, this important bias must be taken into account while deriving population statistics and when selecting sources based on best-fit properties.

As shown in Fig. 5, a large fraction of AGN with $\log L_{2-10, \text{int}} < 44.5$ and $\log N_{\text{H}} > 23$, the sources that produce most of the observed 2–10 keV X-ray background (Buchner et al. 2015; Ananna et al. 2019; Peca et al. 2023), are not detected by Chandra in the CCLS. Thus inferences about N_{H} evolution based on this data set and similarly short observations are model dependent and potentially biased, having to rely on the much deeper, but much smaller solid angle, fields of the CDF-N and CDF-S.

Our methodology of placing the local AGN population on a patch of sky into the high-redshift universe does not account for any potential change to the intrinsic population of AGN over cosmic time. Many X-ray surveys report an increase in the fraction of obscured AGN, and a decrease in the overall AGN number density, with redshift (e.g., Franca et al. 2005; Treister & Urry 2006; Ceca et al. 2008; Hasinger 2008; Ueda et al. 2014; Aird et al. 2015; Lanzuisi et al. 2018; Ananna et al. 2019; Peca et al. 2023; Matthee et al. 2024). In Fig. 9, we show how the measured obscured fraction compares with the simulated population, in bins of both redshift and intrinsic 2–10 keV luminosity. This demonstrates the biases that can occur in X-ray modeling of mildly obscured populations of AGN. The X-ray fitting techniques tend to overestimate the obscured fraction at higher redshifts and at higher luminosities. This leads to a systematic overestimate of the increase in obscuration with redshift and of the obscured fraction at higher luminosities.

Surprisingly, the BAT AGN luminosity analogs redshifted into COSMOS are very similar to the high redshift population when folded in with the measurement biases despite being at $z = 0$. This suggests that the trend of increasing obscuration with redshift may be much less significant than previously believed. Since the increase in N_{H} with redshift has been corroborated in other wavelengths, including by ALMA millimeter wavelength studies of host galaxy contributions (e.g., Gilli et al. 2022), it is unlikely that the increase is in

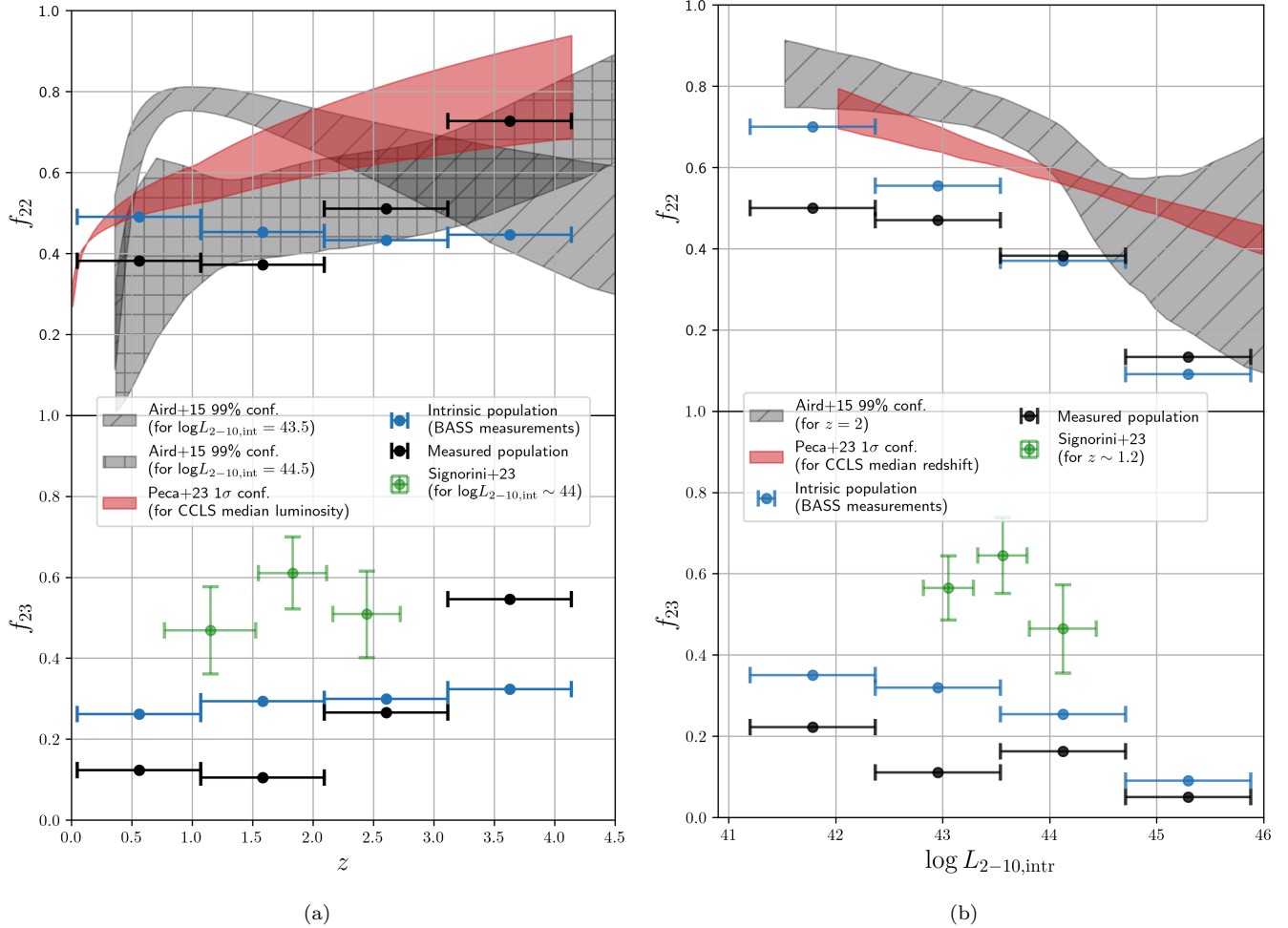


Figure 9. Implications for the evolution of the obscured fraction. These plots show the implication of our study for the cosmic evolution of obscured AGN. f_{22} and f_{23} indicate the fraction of obscured $\log N_{\text{H}} \geq 22$ and $\log N_{\text{H}} \geq 23$ AGN in each bin, respectively. The actual N_{H} of the BAT AGN luminosity analogs is shown in blue and the measured population when observed in COSMOS using the fitting of Sec. 3.2 is shown in black. These are overlaid on top of the evolution models from Aird et al. (2015) and Peca et al. (2023) for comparison. Note that those studies only model f_{22} up to $\log N_{\text{H}} = 24$. For the f_{23} plots, we include the measurements of Signorini et al. (2023) for comparison. **(a) Redshift evolution.** The obscured fraction of the luminosity-matched analogs decreases with redshift, but measurement biases show an increasing trend, consistent with other X-ray studies. **(b) Luminosity function.** The obscured fraction of the actual population exhibits a sharp decline with intrinsic 2–10 keV luminosity, while the measured population shows a gentler decline in line with observed samples. Both of these results show the significant biases in measured populations.

doubt, but our study suggests that it is less significant than X-ray surveys suggest due to modeling biases.

Note that the selection effect we are reporting is a result of using the Chandra response files, and not due to any particular spectral fitting. While we have used the CCLS exposure times and matched the selection function below 30 counts to mimic the effect of CCLS background, any flux-limited Chandra survey is expected to exhibit a similar bias. This ultimately stems from low signal-to-noise and limited band pass.

4.2. Overestimated column densities

We found that many of the simulated sources measured to be obscured and CT had overestimated column densities. This problem was most acute for completely unobscured sources (those with $\log N_{\text{H}} \leq 20$), and is at least partially attributable to 2PL fits, as shown for the “false CT” spectra in Sec. 3.5. Upon inspection of these spectra, we find that (as is generally known) the unabsorbed secondary power law, even at a low normalization fraction, effectively compensates for the extreme absorption of the primary power law. If the intrinsic energy at which the obscuring material becomes optically thin is beyond the Chandra energy range, then the fit

can settle on virtually any high N_{H} to accommodate just a few data points and then use the secondary power law to recover the unobscured continuum. Effectively, for an unabsorbed source, the N_{H} of the primary component is degenerate with the normalization of the secondary component (as noted by Treister et al. 2009). Note that this has the added effect of potentially inflating estimates of X-ray luminosity.

Furthermore, because of the reflection and reprocessing of X-ray photons that shine from the corona onto broad-line region, torus, and accretion disk, spectra often exhibit a high energy ‘‘Compton reflection hump’’ peaking at a rest frame energy of 20–40 keV (Reynolds 1999). For false CT spectra with $z \gtrsim 2$, this may explain the excess flux at the hard end of the Chandra sensitivity band for high redshift sources, which the 2PL fit misinterprets as a hump where the primary component dominates over the secondary. Peca et al. (2021) point out that for low count data in this regime, the effective area also plays a role, since the effective area of Chandra decreases dramatically below 2 keV, particularly in the later years of the mission (see Fig. 11), and at $z \gtrsim 2.5$ the 7.1 keV Fe absorption edge falls at $E \lesssim 2$ keV. Thus, even while the fit passes the ΔC criterion for a better-fit statistic, the model lacks a correct physical meaning. Increasing the ΔC criterion from 2.71 to 6.0 reduces the number of false CT sources from 11 to 4, and increasing the criterion to 9.0 further reduces the number of false CT sources to one. Future work studying the addition of a `pexrav` component to model the Compton reflection hump for obscured sources in fitting pipelines like the one adopted in this paper from M16 (e.g., Liu et al. 2017; Peca et al. 2023) may reveal additional improvements.

To faithfully reproduce M16, we set upper and lower limits on the relative normalization of the secondary power law. As has been noted in previous studies (e.g., Marchesi et al. 2016b; Ricci et al. 2017c; Peca et al. 2023), the secondary component of the 2PL should not exceed a few percent of the primary component, and higher normalizations can lead to pathological fits.

It has been previously suggested by Akylas et al. (2006) that AGN at high redshift are likely to have their N_{H} overestimated by Chandra and XMM-Newton. This is either due to inaccurate photometric modeling, or noisy data in the low-energy bins, which for high redshift (i.e., low count) data, can be misinterpreted as significant obscuration in single power law fits. Our study sheds light onto another caveat of N_{H} estimations in high redshift data when a 2PL model is used.

A detailed discussion of how 2PL fits can confuse unobscured spectra for heavily obscured ones, and conse-

quences of allowing extreme values for the relative normalization can be found in Appendix F. We present examples with visualized spectra in Appendix G.

While we followed the particular procedure of M16 here, various permutations of 2PL fits are widely used in spectral modeling of X-ray surveys (e.g., Brightman et al. 2014; Buchner et al. 2015; Liu et al. 2016, 2017; Peca et al. 2023). Each survey differs in the details, but most have a main model that is a single or double power law being applied to low count data in Chandra’s limited band pass, and the fitting bias we report is expected to apply. Our work does not address the potential effects of AGN variability (Czerny et al. 2000), which can also significantly affect AGN obscuration measurements in surveys that stack multiple pointings (Liu et al. 2017). Instead, we quantify the accuracy of a particular family of fitting procedures, assuming some very well-known intrinsic population based on local measurements.

4.3. Implications for the AXIS mission

Our investigation highlights the magnitude of AGN obscuration bias in X-ray surveys at $E < 10$ keV for $z \lesssim 5$, and the need for a next-generation X-ray mission to constrain this parameter space. The Advanced X-ray Imagine Satellite (AXIS; Reynolds et al. 2023) is a NASA Probe mission concept that will achieve an order-of-magnitude improvement over Chandra’s effective area in the 0.2–10 keV band pass (see Appendix A), an almost two orders of magnitude improvement in high angular resolution survey grasp (i.e., field of view at $< 2'' \times$ effective area), and a CCD energy resolution of ~ 150 eV at 6 keV. Its low background due to a low earth orbit, its large collecting area, and high spatial resolution will allow AXIS to significantly contribute to our understanding of AGN populations at high redshifts.

To test the effectiveness of a mission like AXIS in detecting obscured AGN, we re-simulated our data set with the AXIS `.rmf` and field-of-view-averaged `.arf`,⁸ using an exposure time of 375 ks, which corresponds to the proposed AXIS ‘‘medium deep’’ field (Marchesi et al. 2020; Reynolds et al. 2023; Peca et al. 2024). Spectra were loaded into XSPEC and channels with energies 0.5–10.0 keV, where the AXIS detectors effective area will be greatest, were used. We detected at least three counts in 2223/2280 of the simulated sources (97.5%, compared to 67.2% with Chandra) and at least 30 counts in 98/192 (51.0%, compared to 2.6% with Chandra) of those that were CT.

⁸ version from July 2023, <https://blog.umd.edu/axis/>

Fig. 10 compares the AXIS results with our CCLS simulation results. Note that since the simulated data set was generated to match the CCLS luminosity distribution, Fig. 10(a) does not include the many lower luminosity sources that would be detected in such a study. Panels (b)-(d) show that in each bin of N_{H} and luminosity, AXIS detects a larger fraction of sources than does Chandra. This is most notable for obscured and CT sources.

5. CONCLUSIONS

In this study, we set out to answer two questions in deep-field AGN surveys: (1) how effective is Chandra at detecting obscured AGN? and (2) how accurately do we measure the intrinsic spectral properties of the AGN? We employed a novel method of leveraging models of well-understood local AGN from the BASS all-sky survey, and using them as low redshift templates to simulate the higher median redshift CCLS dataset. We carefully filtered the BASS models to accurately match properties of the CCLS sample, allowing us to compare measured values against the known simulated values. This simulation method can easily be used to study other missions and surveys.

Our main findings are:

- Only **67.2%** of all simulated AGN sources were detected (Fig. 5), with fewer than half of obscured and just **8.9%** of Compton-thick (CT) sources identified. Even fewer obscured and CT sources had sufficient counts for rudimentary spectral modeling, highlighting biases in detecting absorbed AGN in deep surveys. While these results were obtained using the CCLS survey depth, similar results should be expected for any flux-limited Chandra survey, since they are attributable to relatively low count data and limited band pass.
- Among spectra recovered with enough counts for spectral modeling with the methodology of M16, column density errors are small but exhibit significant scatter ($\Delta \log N_{\text{H}} = -0.10^{+0.73}_{-1.16}$) (Fig. 6b). Unobscured sources ($\log N_{\text{H},\text{sim}} \leq 20$) often have column densities significantly overestimated, with 11 "false CT sources" misclassified due to limitations in 2PL models. Single power-law models generally estimate column densities at least as reliably as 2PL models in low-count data. Torus models offer improved constraints on column densities for CT candidates and help identify inaccurate 2PL fits.
- Therefore at CCLS survey depths, conclusions about the redshift distribution and fraction of ob-

scured sources may be unreliable depending on the level of bias from non-detections and biased spectral modeling (Fig. 9). Next-generation missions like AXIS, however, would significantly improve overall AGN detection rates from **67.2% to 97.5%** and CT source detection from **2.6% to 51.0%** (Fig. 10).

While the results of our fitting procedure can likely be generalized to studies with similar model setups as M16, caution should be exercised before comparing with more complex models which are encumbered with much stronger assumptions and more complex systematics. Note however, that such models may over-fit Chandra data and are not always justified by the Chandra data quality.

These considerations highlight the limitations of narrow-band low-count X-ray data and oversimplified spectral models suggesting that additional multi-wavelength analyses are critical. For luminous systems that are AGN-dominated in the IR, IR colors and ratios of X-ray to IR flux may give rough estimates of line-of-sight obscuration, though studies of nearby AGN have found a very large scatter (Pfeifle et al. 2022). Another observation from low redshift AGN is that nearly all AGN with a broad $\text{H}\beta$ emission line have low X-ray column densities (94%, $\log N_{\text{H}} < 22$, Koss et al. 2017) though the misclassified population may increase with redshift. Further studies and simulations are needed to find the best way to use broadband X-ray data with SED model fits and priors on model fitting to best estimate X-ray column density.

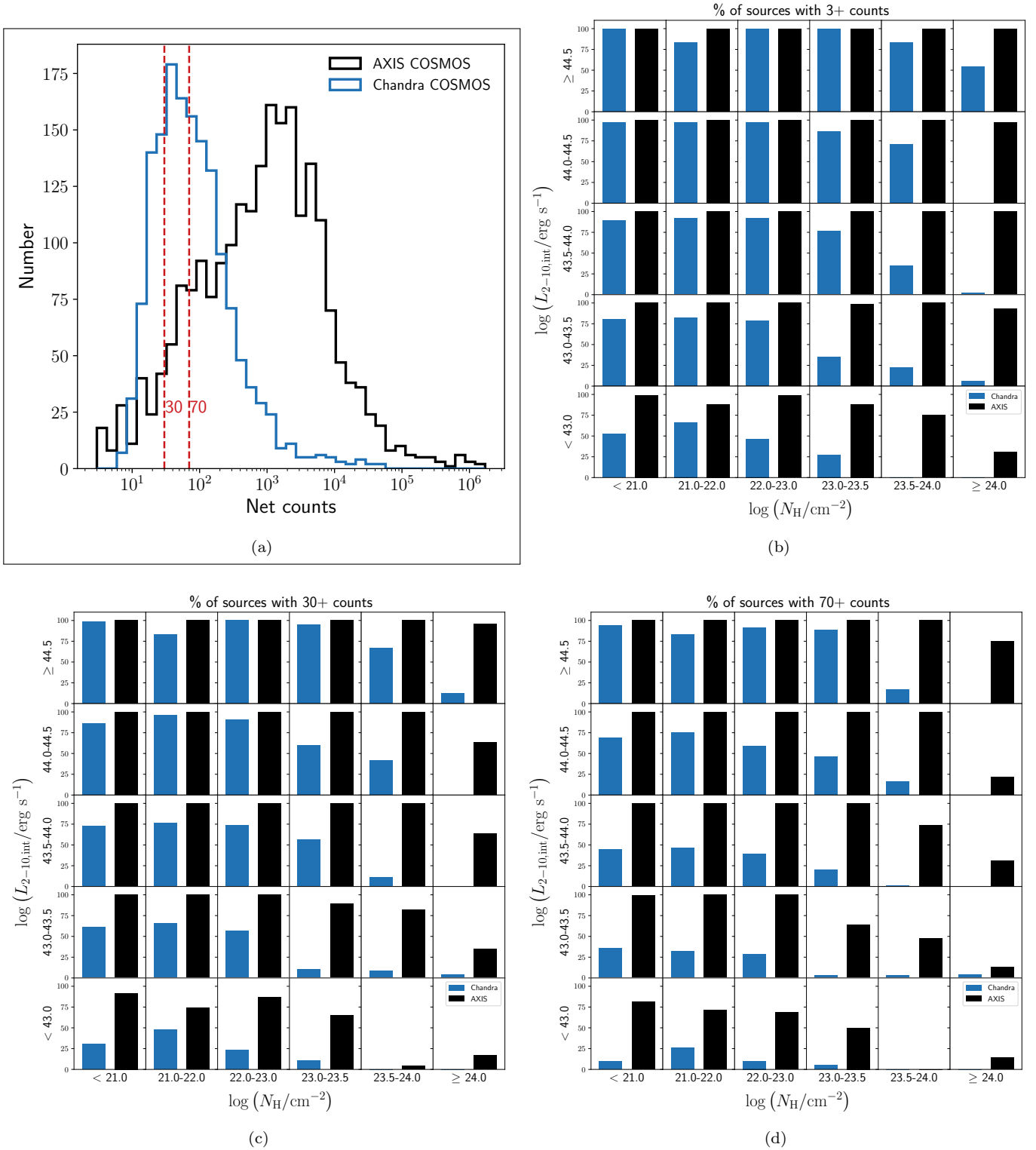


Figure 10. AXIS detections of the simulated dataset organized in bins of intrinsic X-ray luminosity (vertical) and hydrogen column density (horizontal). Contrast with Fig. 5. **(a) Counts distribution.** Distribution of AXIS net counts at 0.5–10.0 keV (black), compared with that of our Chandra simulations at 0.5–7.0 keV (blue). **(b)–(c) Percentage of AXIS simulations with 3+, 30+, and 70+ counts.** The percentage of AXIS simulations in each bin is shown in black, compared with the Chandra percentage in blue.

1 The authors are grateful to: Giorgio Lanzuisi and
 2 Stefano Marchesi for their assistance in understand-
 3 ing the CCLS study and for sharing the CCLS spec-
 4 tra; Laura Blecha, Turgay Caglar, Lea Marcotulli, Ed-
 5 mund Hodges-Kluck, and Meredith Powell for their
 6 valuable insights and feedback; the anonymous ref-
 7 eree for constructive feedback. We acknowledge sup-
 8 port from SAO Chandra archival grant (AR9-20015X)
 9 and NASA through ADAP award 80NSSC22K1126 and
 10 80NSSC19K0749 (M.K.); the Israel Science Foundation
 11 through grant No. 1849/19 (B.T.); the European Re-
 12 search Council (ERC) under the European Union’s Hor-
 13 izon 2020 research and innovation program through grant
 14 agreement No. 950533 (B.T.); FONDECYT Regular
 15 1230345 (C.R), 1241005 (F.E.B., E.T.) and 1200495
 16 (F.E.B, E.T.); ANID grants CATA-Basal FB210003
 17 (C.R., F.E.B., E.T.); Millennium Science Initiative Pro-
 18 gram – ICN12_009 (F.E.B.); Fondecyt Iniciacion grant
 19 11190831 (C.R.); YCAA Prize Postdoctoral Fellowship
 20 and NASA grant 80NSSC22K0793 (M.B.); the China-
 21 Chile joint research fund (C.R.). The work of D.S. was
 22 carried out at the Jet Propulsion Laboratory, California
 23 Institute of Technology, under a contract with NASA.

Software: Astropy (Astropy Collaboration et al. 2013, 2018), XSPEC (v12.11.1; Arnaud (1996))

APPENDIX

A. INSTRUMENT EFFECTIVE AREA

In principle, soft X-ray telescopes should be as effective at detecting obscured AGN as NuSTAR or Swift/BAT for deep surveys, since the rest frame energy of the source increases at higher redshifts. However, to reach energies of 20–30 keV at which heavily obscured sources peak, observations need to be at $z \geq 5$, while CCLS and CDF-S mainly observe sources at $z < 3$. In Fig. 11, we illustrate how the effective area of Chandra at different redshifts compares to that of Swift/BAT at $z = 0$. The dashed lines indicate the energies with peak effective area. Note that at $z = 2$, the median redshift of CCLS, Chandra is still below 20 keV, while at $z = 5$, it begins to overlap with Swift/BAT. Also note that the effective area of Swift/BAT is more evenly distributed across its band pass, while Chandra is preferentially weighted towards detector frame energies below 2 keV. The consequence of this soft weighting and the fact that a typical $\Gamma = 1.4$ power law obscured source will have a factor of 25 more counts at 0.5 keV than at

5 keV means that a flux-limited sample will be highly biased to the softest unobscured sources.

We also include the effective area of AXIS for comparison. Note its order-of-magnitude improvement over Chandra over the entire band pass.

While we focus on effective area in this work, it is important to note that sensitivity, or the minimum detectable flux above background, depends on several factors. These include not only the effective area, but also the background level and the energy range over which the detector operates. For extragalactic surveys targeting faint sources, sensitivity can often be a more critical consideration.

B. BASS MODELS

We briefly summarize the BASS X-ray models that were used as templates to generate our simulation set, as outlined in Sec. 2.2. We refer the reader to R17 Sec. 4 for full details.

The BASS X-ray models were built from broadband spectra using Swift/BAT data in the ultra-hard X-ray band, and combined ASCA, Chandra, Suzaku,

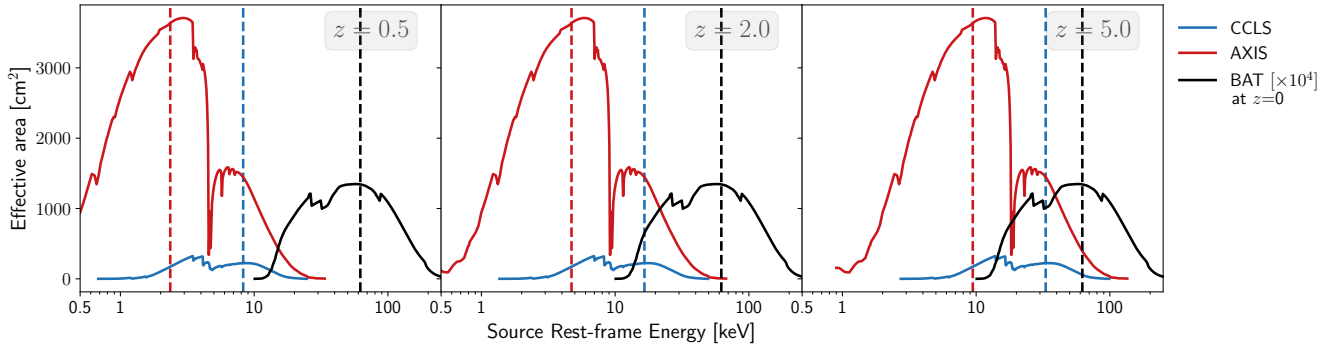


Figure 11. Effective area of Chandra ACIS-I and AXIS as a function of redshift. The effective area of Chandra ACIS-I and AXIS at three different redshifts, compared to that of Swift/BAT at redshift zero. The Swift/BAT curve is scaled by 10^4 for easier visualization. The dashed lines indicate the average energy of the instrument response, weighted by the effective area. The AXIS curves were generated using the field-of-view averaged `.arf`, and the ACIS curves were generated using a representative `.arf` file for a CCLS target (`1id_151`) during Chandra cycle 14.

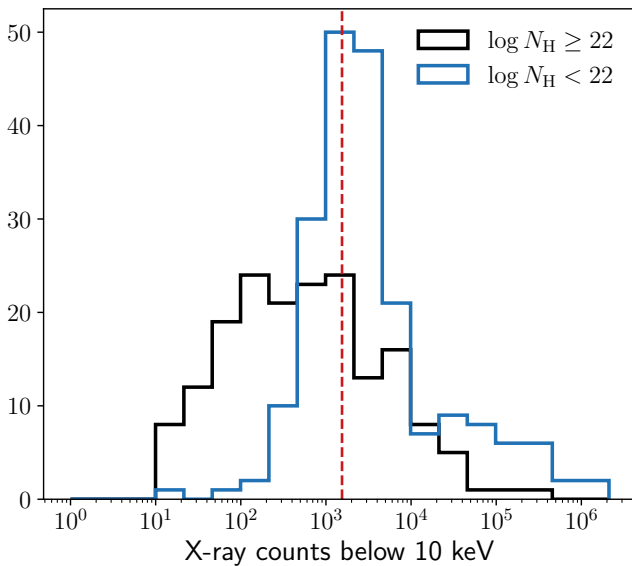


Figure 12. Counts distribution of BASS models used. Photons below 10 keV from which the BASS models were built are from combined ASCA, Chandra, Suzaku, Swift/XRT, and XMM-Newton data. The blue (black) histogram represents the spectra used to build the unobscured (obscured) BASS models for our simulations. A total of 380 models were used. The dashed red line indicates the median of 1545.5 counts.

Swift/XRT, and XMM-Newton data below 10 keV. More details can be found in R17. The counts distribution of the spectra used to build the 380 AGN template models used in our simulations is shown in Fig. 12. The median number of counts is 1545.5. Note that both obscured (black) and unobscured (blue) models are built from high-fidelity spectra.

There are four categories of BASS X-ray spectral models: unobscured (A), obscured (B), blazars (C), and other (D). Since our aim is to simulate the COSMOS

field, we only consider A and B models, which have eight and nine variants, respectively. All variants of these models include the following XSPEC components: `tbabs` (to model Galactic absorption), `constant` (cross-calibration constant to normalize between different instruments), `zphabs`, `cabs`, and `pexrav`. Variants of model A include at least one of the following XSPEC components: `zxicf`, `zpcfabs`, `bbody`, and `apec`. Variants of model B include at least one of the following XSPEC components: `zxicf`, `zpcfabs`, `cutoffpl`, `apec`, and `constant*cutoffpl`. In A models, the reflection parameter of `pexrav` was set to be non-negative in order to take into the account the primary X-ray emission and reprocessed radiation at the same time. In B models, the reflection parameter of `pexrav` was set to be negative, since in these cases, the reflection component is disconnected from the primary X-ray emission and assumed to be unobscured.

A `zgauss` component representing the narrow Fe $K\alpha$ line was added to all spectra for which it could be constrained. 297/698 of the BASS template models, and 163/380 of the models selected for simulations, had a Gaussian component to represent the narrow Fe $K\alpha$ line.

The typical errors in $\log N_{\text{H}}$ and Γ for these models is shown in Table 3.

C. SIMULATED VS. CCLS* COLUMN DENSITY DISTRIBUTION

We did not attempt to match the CCLS* N_{H} distribution in our simulated data set. While this has the potential drawback of not being able to correct the sample size to account for sources missed due to obscuration in the CCLS* sample, it allows us to remain agnostic as to the obscuration bias that we are attempting to measure. The emphasis of this paper is that, assuming some intrinsic N_{H} distribution, which we draw from the

Table 3. Typical errors in the 380 selected BASS models. Each entry shows median value of the width of the 90% confidence interval, and the values within which the medians of 68% of models lie. Note that the width of the $\log N_{\text{H}}$ confidence interval is in logarithmic space. Also note that since all sources in the BASS catalog with $\log N_{\text{H}} \leq 20$ are considered to be consistent with zero, many of the unobscured sources have zero width in the $\log N_{\text{H}}$ measurement.

	Total	$\log N_{\text{H}}$ width	Γ width
$\log N_{\text{H}} < 22$	204	$0.000^{+0.360}_{-0.000}$	$0.240^{+0.210}_{-0.140}$
$22 \leq \log N_{\text{H}} < 23$	68	$0.170^{+0.140}_{-0.100}$	$0.395^{+0.535}_{-0.165}$
$23 \leq \log N_{\text{H}} < 24$	76	$0.200^{+0.140}_{-0.100}$	$0.590^{+0.480}_{-0.240}$
$\log N_{\text{H}} \geq 24$	32	$0.345^{+0.595}_{-0.205}$	$0.450^{+0.220}_{-0.250}$
ALL	380	$0.130^{+0.230}_{-0.130}$	$0.340^{+0.390}_{-0.210}$

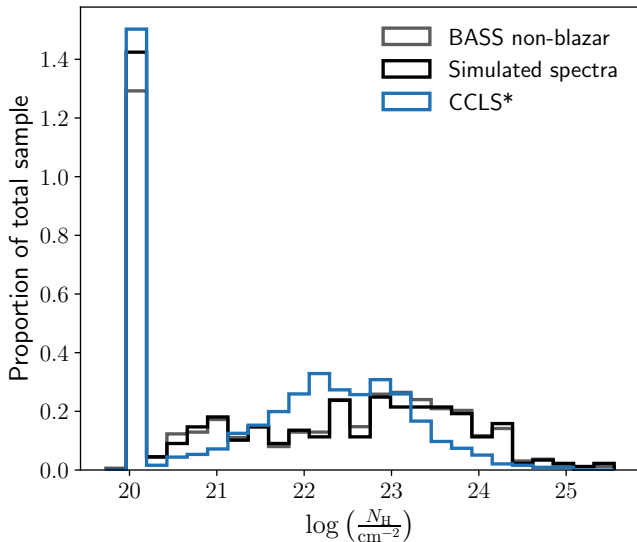


Figure 13. N_{H} distributions of the simulated sample and CCLS. The N_{H} distribution of the BASS models selected for simulations (black) is compared with that of the CCLS (blue). The latter N_{H} distribution was obtained as described in the text. We also include the entire sample of BASS non-blazar AGN (gray). The bin at $\log N_{\text{H}} = 20$ includes all sources with $\log N_{\text{H}} \leq 20$.

local BASS population, the recovered obscured fraction is different and quantifiable as a function of N_{H} and luminosity. A comparison of the simulated and CCLS* N_{H} distributions is shown in Fig. 13. The CCLS histogram in the figure was obtained from M16, after filtering out all Galactic sources and those with undetermined redshift. We replaced the N_{H} of all sources in that catalog that were refit in Lanzuisi et al. (2018) (the ‘‘CT candi-

dates’’) with the updated values. These 1855 sources are a subset of the 2291 that comprise CCLS*. A minimum value of $\log N_{\text{H}} = 20$ was imposed for direct comparison between the samples. We also include the full catalog of BASS non-blazar AGN and note that the 380 selected models are drawn evenly from the N_{H} distribution of entire BASS catalog.

D. POISSON NOISE AND BACKGROUND

In this appendix, we discuss the potential selection effects introduced by the *fakeit* procedure, as well as the effect of background photons on our results.

D.1. *fakeit* procedure

To test the selection effects endemic to the *fakeit* procedure itself, we re-simulated all 2280 spectra, but as simple absorbed power laws ‘*phabs*zphabs*zpow*’. The column density, photon index, and intrinsic luminosity were set by the BASS model, while Galactic absorption, norms, redshift, and exposure times were set as described in Sec. 2.2. We ignored any Gaussian component. Even though this is not an ideal model for heavily obscured AGN, the point of this test is to see how the Poisson noise introduced by *fakeit* affects the ability to recover parameters and not necessarily to accurately model AGN.

1215 of these simulated spectra had at least 30 counts, and we fit these using only the first two steps of the fitting procedure from Sec. 3.2. Since the same model was used in both the simulations and the fits, any error in recovering parameters is due to low counts and the introduction of Poisson noise alone.

N_{H} was accurately fit to 90% confidence for 1098/1215 (90.4%) of all fits, in 812/874 (92.9%) of all unobscured simulations, 286/341 (83.9%) of all obscured simulations, and 7/7 (100%) of all CT simulations. The accuracy of N_{H} measurements seems to correlate more with counts than with obscuration: 215/253 (85.0%) of simulations with fewer than 50 counts, 310/351 (88.3%) of simulations with 50–99 counts, 153/169 (90.5%) of simulations with 100–149 counts, and 420/442 (95.0%) of simulations with at least 150 counts were measured accurately to 90% confidence. Note that in the study presented in this paper, N_{H} was accurate to 90% confidence in 85.3% of fits, and accuracy did not correlate with counts.

D.2. Background photons

Background photons are not included in the simulations, and therefore we do not subtract the background of the simulated spectra or do background spectral modeling. When determining the detection fraction, we compute the net counts in each simulated spectrum and

compare it with the predetermined threshold of three counts. We expect many spurious sources with at least three counts, and the additional cut that we perform in Sec. 3.1 for sources with fewer than 30 counts can be interpreted as a comparison with a galaxy catalog or some other cross-reference validation.

For the Chandra ACIS-I detector in cycle 14, the background rate in the 0.5–7.0 keV band for a $2''$ detection radius⁹ with aperture correction is $\sim 9 \times 10^6$ cts/s = 1.4 cts per aperture on average in 160 ks. Based on the confidence limits in Table 1 of Gehrels (1986), a 3σ detection with 1.4 background counts requires ~ 12 net counts. Note that even zero background photons would require seven counts for a detection, so the three count detection criterion results in a conservative overestimate for our detection fraction. Moreover, according to Fig. 9 of Civano et al. (2016), $> 99\%$ of the sample has $\gtrsim 6$ counts in the 0.5–7.0 keV band and $\sim 90\%$ have $\gtrsim 10$ counts. We compensate for this likely overestimate by matching the CCLS counts function for detections of fewer than 30 counts.

Civano et al. (2016) use the CIAO WAVDETECT tool (Fruscione et al. 2006) to determine detected sources, and accept a false-positive detection probability that corresponded to about 10 in every 150 sources ($\sim 7\%$). This corresponds to a detection threshold of about 8 counts for an average of 1.4 background counts per $2''$ aperture.

We do not expect our spectral fitting results to be significantly affected by the lack of background. Using Poisson statistics,¹⁰ if we again assume a mean of 1.4 counts per aperture, then out of 2280 sources (the number of simulations we generated) we expect (562, 787, 551, 257, 90, 25, 6, 1) systems with (0, 1, 2, 3, 4, 5, 6, 7, 8) background counts in their apertures, or a 5% chance of a source having at least five background counts. Since we only modeled spectra with at least 30 counts, and our conclusions about fitting results apply just as well to spectra with thousands of counts, we do not expect the lack of background to significantly bias our spectral fitting.

E. FITTING STATISTICS

The fit statistics for the 1179 fitted simulations are shown in Fig. 14. The reduced C statistic, defined as C divided by degrees of freedom, is a goodness of fit metric. The reduced value $C \sim 1$ implies a good fit. Reduced $C < 1$ (> 1) implies an under-determined

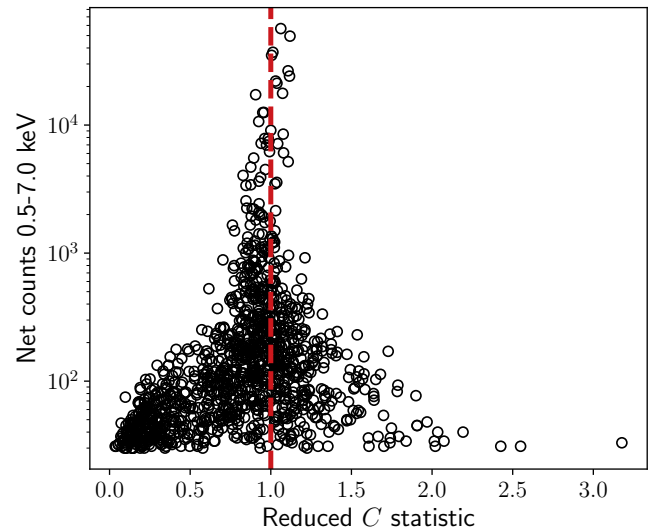


Figure 14. Fitting statistics for the simulated data set. The reduced C statistic is shown along with the net counts of each simulated spectrum. The red dashed line is drawn at 1. The excess of under-determined fits ($C < 1$) for simulations with fewer than 70 counts may be due to the lack of background in our study.

(over-determined) fit. The median reduced C is 0.87 for sources with at least 30 counts and 0.93 for those with at least 70 counts. The standard deviations are 0.39 and 0.26, respectively. An excess of under-determined fits is largely due to spectra with < 70 counts. This may be because we did not simulate or model a background spectrum. This distribution did not change significantly with the more stringent criteria (ΔC of 6.0 and 9.0).

F. DETAILED DISCUSSION OF DOUBLE POWER LAW MODEL

Here we discuss the effectiveness of a 2PL for capturing AGN obscuration in X-ray spectra.

F.1. Why a secondary power law?

The primary power law ($KE^{-\Gamma}$) continuum is observed in the CCLS redshift range at 0.5–20 keV, and since finer features of the spectrum cannot be recovered in low signal-to-noise data, this is what is modeled for basic fits. When there is a high column density ($\log N_{\text{H}} \gtrsim 20$), the power law is multiplied by factors of $e^{-N_{\text{H}}\sigma(E)}$, where $\sigma(E)$ is the photoelectric cross section that depends on both energy and species, to account for absorption (Morrison & McCammon 1983). However, even in obscured cases, there are often photons at energies below the photoelectric cutoff due to photons leaking through the obscuring material and other factors (the physical cause of this soft component is discussed in many papers, including in, e.g., Secs. 4.1.3 and 5.4.2 of

⁹ According to Fig. 2 of Civano et al. (2016), most of the sources lie in an aperture of $2''$ – $4''$. $2''$ thus represents the edge of the bin.

¹⁰ $P(X = k) = e^{-\lambda} \lambda^k / k!$ for a mean and variance of λ .

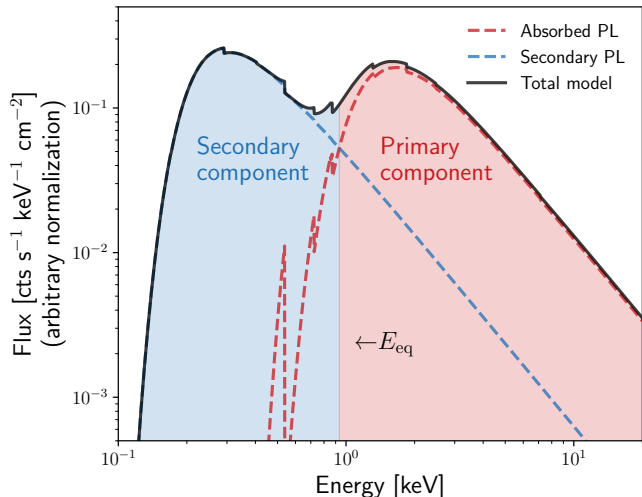


Figure 15. Double power law model. A typical 2PL model with an obscured primary component (red) and an unobscured secondary component with an identical slope (blue). Here the normalization of the secondary component is chosen to be 5% of the primary normalization. The main feature of this model is the “hump” at which the primary component begins to dominate over the secondary component. E_{eq} is the energy at which the two power laws are equal, and above which the primary component dominates.

R17 and in Gupta et al. 2021, for BASS AGN). A single power law can then fit these soft photons simultaneously by underestimating N_{H} and lowering the power law index Γ , giving a relatively flat model with an inaccurate physical interpretation. To remedy this while still minimizing the number of fit parameters, a secondary, unobscured power-law component can be added. Since the soft photons are believed to be sourced from the same coronal emission, the index of the secondary power law is tied to that of the primary, and the normalization can either be free to vary, or even fixed to some fraction of the primary normalization (effectively assuming some coupled covering and scattering fraction for the obscuring material) to maintain the same number of free parameters (e.g., Ueda et al. 2007). This fraction is typically on the order of a few percent (e.g. M16, R17, Bianchi & Guainazzi 2007; Gupta et al. 2021; McKaig et al. 2023; Peca et al. 2023). The 2PL thus provides a model that is more physically accurate than a single power law while still accommodating low-count data because it has few free parameters when it is statistically required.

F.2. Column density degeneracy

The main feature in an absorbed spectrum modeled by a 2PL is the “hump” where the primary obscured power law dominates over the unobscured secondary power law. The location of the hump is determined by

the N_{H} of the model. For low column densities, the hump coincides almost exclusively with the peak of the secondary component; as N_{H} increases, the hump separates from the peak of the secondary component and moves toward higher energies. We define the energy at which the two power laws are equal, and after which the primary component dominates, as E_{eq} , as shown in Fig. 15

As a result, for a given detector band pass, each redshift determines a range of N_{H} values that can or cannot be captured by a 2PL (assuming high fidelity data throughout the detector band pass). If E_{eq} is at or above the high end of the sensitivity band, too few photons from the primary component are detected and N_{H} is unconstrained from above. If E_{eq} is at or below the low-energy sensitivity cutoff, then the secondary component is not sufficiently represented, then N_{H} is unconstrained from below. Thus there is a degeneracy between a single power law and 2PL model if E_{eq} is outside of the detector band pass, since in these cases, the spectrum will appear as a single, unabsorbed power law. This can be interpreted as either the primary component of a relatively unobscured spectrum or as the soft leakage from a highly obscured source. The degeneracy is further exacerbated by the Compton reflection hump that is often observed in X-ray spectra—a slight excess at the hard end of an unobscured spectrum can be interpreted as the hump of the primary component in a highly obscured spectrum at high redshift. These degeneracies are of less concern in broadband spectra, which cover a wider range of E_{eq} in the detector sensitivity band.

We illustrate this phenomenon in Fig. 16. The vertical dashed lines indicate E_{eq} for different values of $\log N_{\text{H}}$, and the shaded regions are beyond the 0.5–7.0 keV band pass of Chandra. For each redshift panel, we expect spectra with N_{H} values whose E_{eq} is within the white region to be well-recovered by a 2PL. Note that E_{eq} is a function of the secondary power law normalization; here we have assumed a value of 5%, consistent with the upper limit of the prescriptions in M16 and R17.¹¹

To quantify this limitation of the 2PL fit, we compute a “primary ratio” (PR), which we define as

$$\text{PR} = \frac{n_{\text{p}} - n_{\text{s}}}{n_{\text{p}} + n_{\text{s}}}, \quad (\text{F1})$$

¹¹ This model only accounts for photoelectric absorption in the primary component. Note that at $N_{\text{H}} \gtrsim 10^{23}$, Compton scattering suppresses it significantly further. This effect is taken into account by the XSPEC `cabs` model. However, our goal here is to evaluate the merits and faults of the 2PL as used in studies like M16.

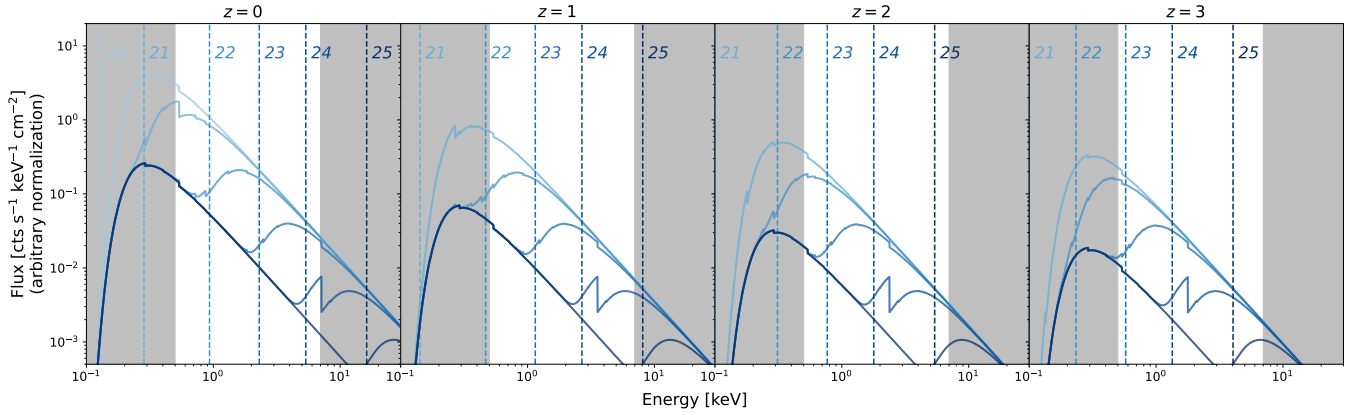


Figure 16. Double power laws at varying redshift and N_{H} . We overlay a 2PL model onto the Chandra energy band, at four redshifts. The vertical dashed lines indicate E_{eq} , the energy at which the primary power law equals the secondary power law, and beyond which the primary component dominates. The shaded regions are beyond the Chandra energy band. For each redshift, the N_{H} values for which E_{eq} is well within the white region are the N_{H} values that we expect to be well-recovered by a 2PL model. Other N_{H} values are subject to degeneracy between a heavily obscured model with a significant secondary component and an unobscured single power law.

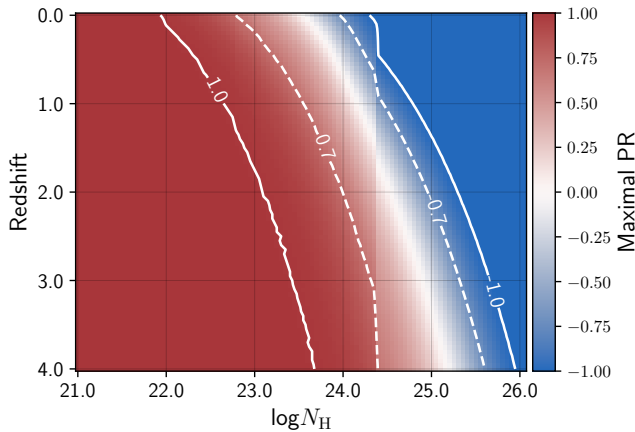


Figure 17. Primary ratio as a function of redshift and N_{H} . We compute the maximal primary ratio, as defined in the text, for CCLS simulations using a 2PL model with a 5% secondary normalization at a range of redshifts and N_{H} . We used the CCLS response files and a high exposure time of 10^{12} s to minimize Poisson noise and accurately measure the ratio. The area between the white lines is where the 2PL is expected to accurately recover N_{H} at a given redshift, assuming high fidelity data. Outside of the solid white lines (PR = ± 1), only a single power law is detectable, which can be interpreted as either the secondary component of a highly obscured source or the primary component of an unobscured source. The discontinuity at $\log N_{\text{H}} \sim 24.3$ is due to the absorption edge in the detector response that can be seen in the $\log N_{\text{H}} = 24$ models of Fig. 16.

where n_{p} is the number of primary component photons ($E > E_{\text{eq}}$) and n_{s} is the number of secondary component photons ($E < E_{\text{eq}}$). PR close to +1 (-1) indicates that nearly all detected photons are from the primary (secondary) component. For a given model, we can cal-

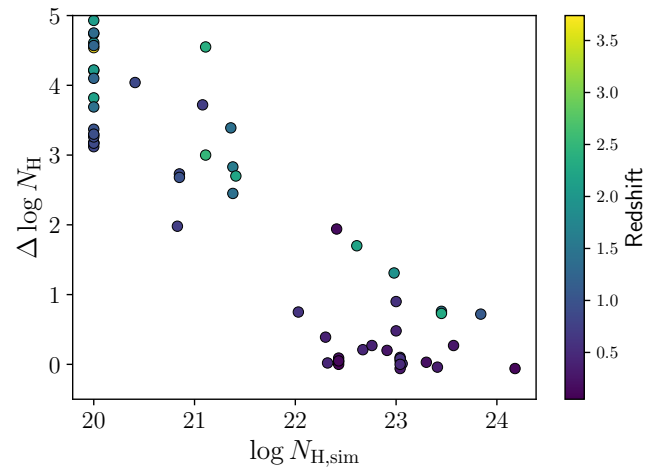


Figure 18. N_{H} accuracy of the double power law fits as a function of $N_{\text{H},\text{sim}}$ and z . Among the 60 simulated spectra that were fit to a 2PL, those with $z < 1$ begin to accurately measure N_{H} for column densities of $\log N_{\text{H}} \gtrsim 22$, while the higher redshift simulations ($z \gtrsim 2$) are measured accurately within 1 dex for $\log N_{\text{H}} \gtrsim 23$. This is consistent with the predictions of the heatmap in Fig. 17. Note that the ability of the 2PL to accurately estimate N_{H} depends on the actual PR, while the heatmaps predict the maximal PR for a given model. This explains the low redshift fits at higher $\Delta \log N_{\text{H}}$.

culate the “maximal PR,” the theoretical PR assuming high quality data simulated from the model, and then given data, we can also calculate the actual PR once E_{eq} is computed from the model. The actual PR is what indicates the validity of the fit (see example in Sec. G.2). We expect that the closer a PR is to zero, the better-suited a 2PL model is to fitting the spectrum. PR is a function of the detector response, the detector

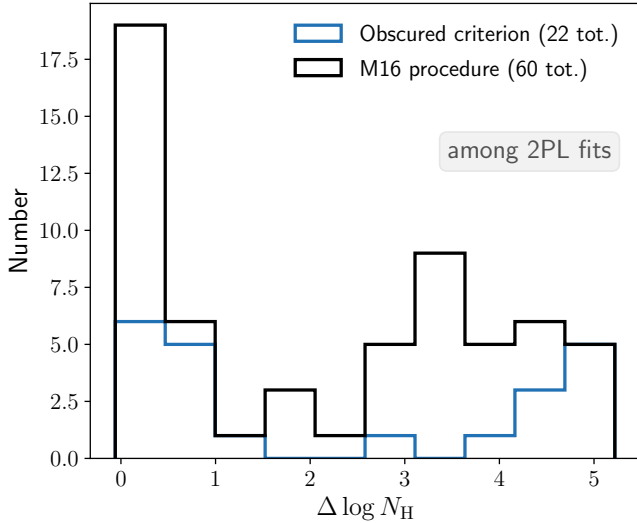


Figure 19. N_H accuracy of the double power law fits using the obscuration criterion. A comparison of the ΔN_H histograms for the 2PL fits in the original procedure (black) and when only attempting the 2PL model for sources with the additional criterion that the single power law estimates $\log N_{H,\text{meas}} \geq 23$ (blue). While the obscured criterion yields fewer fits with moderately overestimated N_H , the criterion does not suppress severely overestimated N_H sources.

band pass, the secondary normalization, redshift, and N_H . We simulate a 2PL spectrum with a 5% secondary normalization using the CCLS response files, and compute the maximal PR for a range of redshifts and N_H . The results are shown in Fig. 17.

We test this understanding by looking at our simulated data set. Among those simulations that settled on a 2PL, we look at $\Delta \log N_H$ as a function of $N_{H,\text{sim}}$ and redshift. According to Fig. 17, simulations for $z \sim 0$ should only be accurate for $\log N_{H,\text{sim}} \gtrsim 22$, with the threshold increasing at higher redshifts, assuming the highest-possible data quality. Indeed, this expected trend can be observed in Fig. 18. This prediction is also consistent with the example spectrum presented in Sec. G.1: the simulated and measured N_H values are on opposite sides of the solid white lines of Fig. 17 for the redshift of the simulation.

One potential way to break this degeneracy is to only try the 2PL fit for spectra that are measured to be obscured by a single power law fit. We refit all spectra according the M16 procedure outlined in Sec. 3.2, but with the additional check that step 3 (the 2PL fit) was only performed if $\log N_{H,\text{meas}} \geq 23$ to 90% confidence after that power law fit. 22/60 2PL fits, and 9/11 false CT, remained.

Fig. 19 compares the N_H accuracy of 2PL fits with and without this additional criterion. While the criterion succeeds in suppressing moderately overestimated N_H fits, it still results in many sources with $\Delta \log N_H \gtrsim 4$, all of which are completely unobscured. The fits with $1 \lesssim \Delta \log N_H \lesssim 4$ turn out to be primarily sources with $20 < \log N_{H,\text{sim}} < 23$. If the criterion is made even stricter such that step 3 is only performed if the best-fit $\log N_{H,\text{meas}} \geq 23$, then, by construction, the 2PL only overestimates N_H for those sources which the single power law also overestimates, but we find that there is no improvement in accuracy.

After studying different scenarios with the 2PL, including setting a lower threshold for the secondary normalization and stricter ΔC criteria, we find that with the limited band pass of Chandra, a single power law always estimates N_H at least as well as a 2PL.

F.3. Normalization of the secondary power law

As noted in previous studies (e.g., Marchesi et al. 2016b; Ricci et al. 2017c; Peca et al. 2023), the secondary component of the 2PL should not exceed a few percent of the primary component. The methodology developed for this study presents an opportunity to explore this additional important limitation of the 2PL. When we repeated our fitting procedure from Sec. 3.2, but without any constraints on ‘constant.factor’ in the 2PL, we found 243/1179 2PL fits, compared with 60/1179 when we imposed upper and lower limits. We found 53 false CT sources (see Sec. 3.5), compared with 11 in our study, and again, each of them settled on 2PL fits. Among them, 17 had relative normalization $> 15\%$ and six had a relative normalization $< 0.001\%$.

In the case of a high secondary normalization, the depression between the primary and secondary power laws is shallow, and the secondary power law can be used to fit a few noisy data points to an unabsorbed spectrum, and the model no longer physically represents an obscured AGN X-ray continuum. Each of the four fits with secondary normalizations greater than 50% were relatively high signal-to-noise spectra (> 150 counts—these can be fit to more sophisticated models). An example of a nonphysical 2PL fit with a high secondary normalization is shown below in Sec. G.3.

In the case of a very low secondary normalization, there are two factors that can make the model nonphysical. The first is that arbitrarily low relative normalizations can couple with arbitrarily high normalizations, and arbitrarily high N_H for the primary power law, resulting in the secondary component filling the entire band pass. The second is that, for relatively low count data, when primary normalizations that are physical,

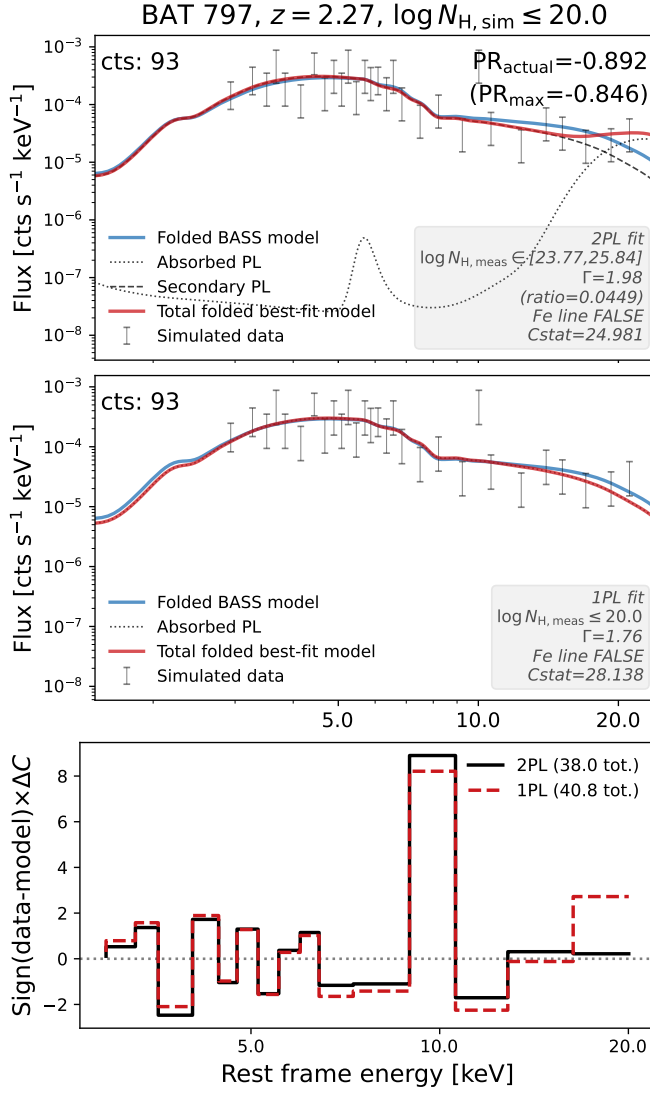


Figure 20. False CT example 1: high redshift with a bump. See Appendix G for an explanation of the panels and Sec. G.1 for a discussion of this example.

extremely low flux corresponds to low signal-to-noise, and is not physically significant. An example of a non-physical 2PL fit with a low secondary normalization is shown below in Sec. G.4.

F.4. Prescriptions

To ensure that 2PL models accurately estimate the N_{H} of AGN spectra, it is important to consider the source redshift, the detector band pass, and the slope of the continuum, all of which determine the severity of the degeneracy between unobscured and heavily obscured spectra. This is quantified by the PR metric, which determines the regions of parameter space within which we expect the 2PL model to accurately measure N_{H} . For fixed Γ , and secondary normalization, the Chandra band

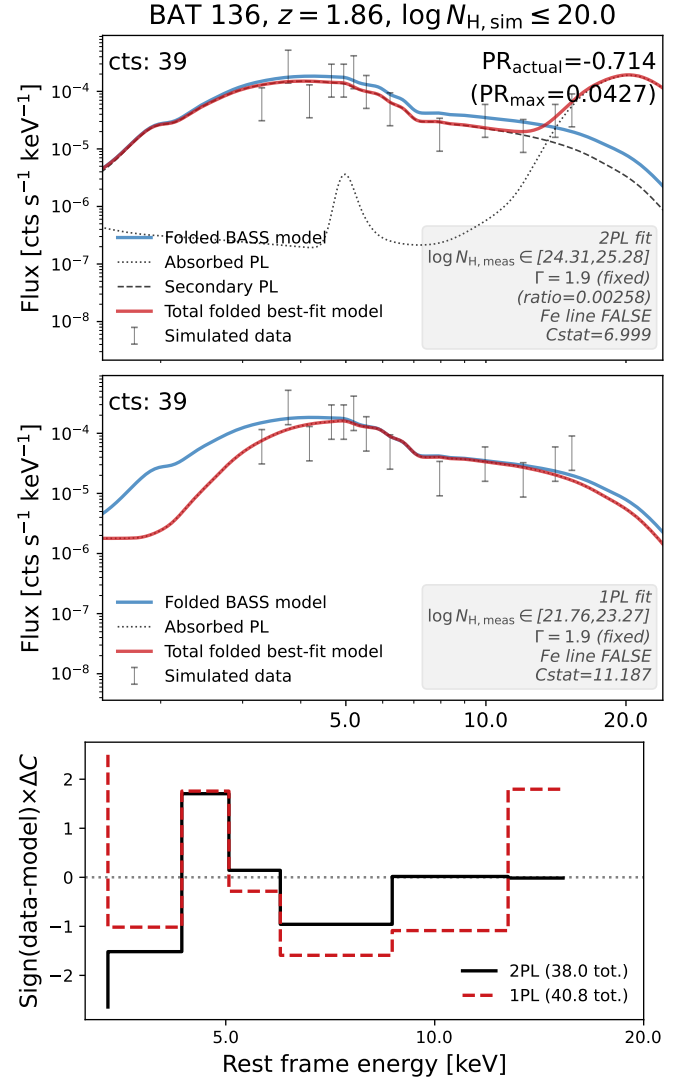


Figure 21. False CT example 2: out of band pass, few photons. See Appendix G for an explanation of the panels and Sec. G.2 for a discussion of this example.

pass allows for a range of N_{H} approximately 2 dex wide at each redshift for the which the 2PL is appropriate, as illustrated in Fig. 17. Outside of that range there is degeneracy between very low and very high column densities. Furthermore, while a given 2PL may have a suitable maximal PR, the actual PR based on the data may be poorer.

A 2PL model should also be avoided for spectra with high signal-to-noise spectra, where more degrees of freedom can be employed. Often, careful visual inspection, testing with different ΔC criteria, and testing with different limits on the secondary normalization can reveal nonphysical fits.

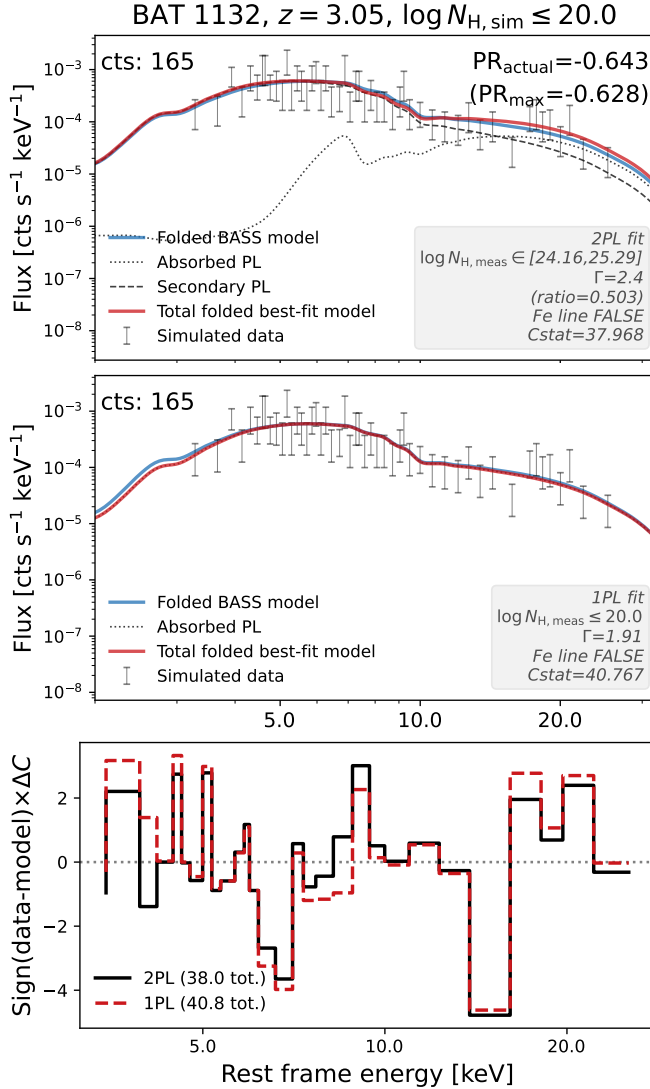


Figure 22. False CT example 3: high secondary normalization. See Appendix G for an explanation of the panels and Sec. G.3 for a discussion of this example.

G. ILLUSTRATIVE EXAMPLES OF FALSE CT SOURCES

Here we provide a description of Figs. 20–23, each of which show illustrative examples of false CT sources. In the top panels, the simulated spectrum is shown as error bars showing each bin’s Poisson error of flux. All spectra are binned to a minimum of three counts per bin. The blue solid curves show the BASS template from which the spectrum was simulated, the dotted and dashed lines show the best-fit model components, and the red solid curve shows the total fit model. The best-fit parameters are shown in the gray text boxes. $\log N_{\text{H}, \text{meas}}$ shows the 90% confidence interval for the measured intrinsic obscuration in the case that the spectrum was

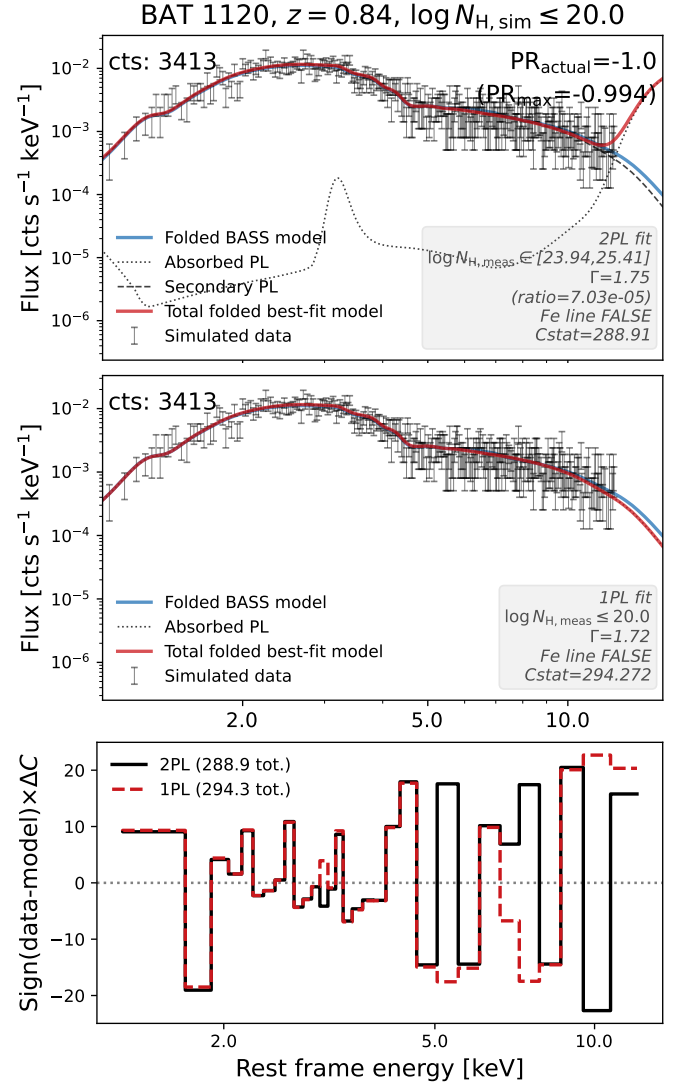


Figure 23. False CT example 4: low secondary normalization. See Appendix G for an explanation of the panels and Sec. G.4 for a discussion of this example.

to have $\log N_{\text{H}, \text{meas}} > 20$. Note that $\log N_{\text{H}} \leq 20$ is consistent with zero.

Top: The 2PL fit settled on by the fitting algorithm described in Sec. 3.2. This fit overestimates the N_{H} of the completely unobscured simulation, since the secondary power law can compensate for the extreme absorption of the primary component. Both the actual and maximal primary ratios (PR, see Appendix F) are shown on the top-right of the panel. Note that $|\text{PR}_{\text{actual}}|$ close to unity indicates that a 2PL model cannot, in principle, recover N_{H} in these cases. Further note that while a model may in principle have a maximal PR close to zero,

the data quality ultimately determines the actual ratio of primary to secondary photons.

Middle: The fit when a secondary power-law component is not allowed, which more accurately measures N_H despite a higher overall C statistic.

Bottom: Comparison of the contribution to the fitting statistic in each energy bin. In each case, the 2PL (black) has an overall lower C statistic than the single power law (red dashed). These panels are adaptively binned for easier visual inspection.

G.1. *Example 1: high redshift with a bump*

Our first false CT example is shown in Fig. 20. In this example, there is a slight bump at the high-energy end that the 2PL captures. By comparing the data with the BASS model (blue), it is seen that this bump is due to Poisson noise. The residual plot in the bottom panels shows that the high data point at the end contributes most to the more favorable C statistic of the 2PL over the single power law. Note that a similar effect may occur in AGN spectra with a Compton reflection hump. This example illustrates the degeneracy between $\log N_H \lesssim 23$ and $\log N_H \gtrsim 25.5$ for $z = 2.27$ shown in Fig. 17. Note that even spectra with $\gtrsim 100$ counts are subject to this degeneracy. The PR of -0.892 quantifies the dominance of secondary photons over primary photons in this 2PL model. The single power law in the middle panel accurately classifies this source as unobscured, and by visual inspection can be seen to recover the template model with high accuracy, despite the higher overall C statistic.

G.2. *Example 2: out of band pass, few photons*

Our second false CT example is shown in Fig. 21. This example illustrates how visual inspection of spectra can reveal obvious mismatches to data that are not captured in fitting statistics, since the model clearly suppresses the primary power law just enough to push it out of the band pass of this data. This leaves only the unobscured secondary component in the band pass, which is equivalent to fitting to just a single unobscured power law. Here we see a case where, in principle, the 2PL model should be able to discern the best-fit $N_{H,meas}$ ($PR_{max} \sim 0$), but the paucity of photons in the actual data render the 2PL insufficient ($|PR_{actual}| > 0.7$). Although the best-fit $\log N_{H,meas}$ for the single power law is still an overestimate for this simulation, it performs significantly better. It is easy to see the cause of this overestimate: two of the first three bins fall below the model curve due to random noise. At high redshift, any small dip in the spectrum represents a very high obscuration because it's a higher energy bin intrinsically.

Note that this example would still be incorrectly fit for a more stringent ΔC criterion.

G.3. *Example 3: high secondary normalization*

The false CT example shown in Fig. 23 illustrates how a high secondary normalization results in a shallow depression between the two power laws. This allows the model to fit an N_H that would not typically be degenerate at that redshift by a 2PL with an appropriately low secondary normalization and effectively turns the secondary power law into a fudge factor that can slightly improve a fitting statistic. Indeed, the PR is not quite as high in this example, but the obscuration is still overestimated. Notice that the most improvement to the fit statistic is in the first couple of bins, where the secondary power law boosts the model up slightly to better match the BASS template model.

G.4. *Example 4: low secondary normalization*

In the false CT example shown in Fig. 22, we can see the degeneracy between $\log N_H \lesssim 22.5$ and $\log N_H \gtrsim 24.5$ for $z = 0.84$ shown in Fig. 17. Note that by allowing an extremely low secondary normalization, even very high-fidelity spectra are subject to this degeneracy. This example also illustrates how visual inspection of spectra can reveal obvious mismatches to data that are not captured in fitting statistics, since the model clearly suppresses the primary power law just enough to accommodate the band pass of this data. The secondary power law thus takes up the entire data, indicated by $PR_{actual} = -1$. This is achieved by a combination of an unreasonably high primary normalization ($2.135 \text{ cts keV}^{-1} \text{ s}^{-1} \text{ cm}^{-1}$ at 1 keV, compared with typical values $\lesssim 1 \times 10^{-4} \text{ cts keV}^{-1} \text{ s}^{-1} \text{ cm}^{-1}$ at 1 keV) and an extremely high obscuration of $\log N_H = 25.21$. Note that this example would still be incorrectly fit for a more stringent ΔC criterion. In any case, high-fidelity spectra like this can generally be fit with more sophisticated models.

H. DATA TABLES

Our simulated data set was constructed from 380 BASS AGN template models.¹² The selection of these models is described in Sec. 2.2. Table 4 lists the BAT catalog ID of each model, as well as the six redshifts and exposure times selected for each to generate our simulated CCLS catalog.

Simulation properties and the results of the fitting routine described in Sec. 3.2 are tabulated in Table 5.

¹² The detailed catalog and data can be found at <https://www.bass-survey.com/>

These are the naive fit parameters before any refitting described in the results and discussion sections.

Table 5. Contents of simulation catalog

Num	Label	Units	Explanation
1	batID		BAT ID of source
2	SwiftID		Swift-BAT 70-month hard X-ray survey source name
3	specZ_BASS		Spectroscopic redshift of BASS template source
4	logL2-10-intr_sim	erg s ⁻¹	Logarithm of intrinsic luminosity in the 2–10 keV range of BASS template source
5	logNH_sim	cm ⁻²	Logarithm of column density of the neutral obscuring material of BASS template source
6	Gamma_sim		Photon index of the primary X-ray continuum of BASS template source
7	gauss_sim		Flag for Gaussian in BASS template source
8	z_sim		Redshift of simulated spectrum
9	counts	cts	0.5–7.0 keV net counts of simulated spectrum
10	detection		Detection status of simulated spectrum
11*	logNH_meas	cm ⁻²	Measured logarithm of column density of the neutral obscuring material of simulated spectrum
12	b_logNH_meas	cm ⁻²	Lower bound, 90% confidence interval for logNH_meas
13	B_logNH_meas	cm ⁻²	Upper bound, 90% confidence interval for logNH_meas
14	Gamma_meas		Measured photon index of the primary X-ray continuum of simulated spectrum
15	f_Gamma_meas		Flag on Gamma_meas, indicating a fixed value during fitting
16	b_Gamma_meas		Lower bound, 90% confidence interval for Gamma_meas
17	B_Gamma_meas		Upper bound, 90% confidence interval for Gamma_meas
18	Gamma_ratio_meas		Ratio of Gamma_2 to Gamma_1 in 2PL model of simulated spectrum
19	pl_norm	cts/keV/s/cm ²	Measured norm of the PL
20	gauss_norm	cts/keV/s/cm ²	Measured norm of the Fe line Gaussian
21	cStat_meas		Best fit statistic of simulated spectrum
22	red_cStat_meas		Best fit statistic / dof of simulated spectrum
23	best_fit		Model code for best fit of simulated spectrum
24	error_flag		XSPEC error code for confidence intervals on N_H

* This and all subsequent columns are only for fitted sources, which are those with at least 30 counts

NOTE—Table 5 is published in its entirety in the machine-readable format.

REFERENCES

- Aird, J., Coil, A. L., Georgakakis, A., et al. 2015, *Monthly Notices of the Royal Astronomical Society*, 451, 1892, doi: [10.1093/mnras/stv1062](https://doi.org/10.1093/mnras/stv1062)
- Akylas, A., Georgantopoulos, I., Georgakakis, A., Kitsionas, S., & Hatziminaoglou, E. 2006, *Astronomy and Astrophysics*, 459, 693, doi: [10.1051/0004-6361:20054632](https://doi.org/10.1051/0004-6361:20054632)
- Alexander, D. M., Stern, D., Moro, A. D., et al. 2013, *ApJ*, 773, 125, doi: [10.1088/0004-637X/773/2/125](https://doi.org/10.1088/0004-637X/773/2/125)
- Ananna, T. T., Treister, E., Urry, C. M., et al. 2019, *The Astrophysical Journal*, 871, 240, doi: [10.3847/1538-4357/aafb77](https://doi.org/10.3847/1538-4357/aafb77)
- Annun, A., Alexander, D. M., Gandhi, P., et al. 2020, *Monthly Notices of the Royal Astronomical Society*, 497, 229, doi: [10.1093/mnras/staa1820](https://doi.org/10.1093/mnras/staa1820)
- Arnaud, K. A. 1996, in *Astronomical Society of the Pacific Conference Series*, Vol. 101, *Astronomical Data Analysis Software and Systems V*, ed. G. H. Jacoby & J. Barnes, 17
- Astropy Collaboration, Robitaille, T. P., Tollerud, E. J., et al. 2013, *\aap*, 558, A33, doi: [10.1051/0004-6361/201322068](https://doi.org/10.1051/0004-6361/201322068)
- Astropy Collaboration, Price-Whelan, A. M., Sip\Hocz, B. M., et al. 2018, *\aj*, 156, 123, doi: [10.3847/1538-3881/aabc4f](https://doi.org/10.3847/1538-3881/aabc4f)
- Baloković, M., García, J. A., & Cabral, S. E. 2019, *Research Notes of the American Astronomical Society*, 3, 173, doi: [10.3847/2515-5172/ab578e](https://doi.org/10.3847/2515-5172/ab578e)

Table 4. Template models for the simulated data set. Each BAT ID model was selected based on its intrinsic 2–10 keV luminosity, and simulated at six different redshifts and exposure times. Redshifts and exposure times were chosen as described in Sec. 2.2.

batID	$\log L_{2-10, \text{int}}$ (erg s^{-1})	$\log N_{\text{H}}$ (cm^{-2})	z1	z2	z3	z4	z5	z6	exp1 (ks)	exp2 (ks)	exp3 (ks)	exp4 (ks)	exp5 (ks)	exp6 (ks)
1	43.42	22.19	0.63	0.73	1.01	0.76	1.09	1.56	169.92	71.79	157.76	172.92	170.11	162.63
2	43.61	20.00	1.02	2.56	1.63	0.84	1.94	2.50	27.40	162.74	171.17	268.40	121.21	180.44
4	43.04	22.86	1.00	1.20	1.16	0.95	1.24	0.82	167.36	161.05	36.13	152.89	151.93	154.02
5	44.01	22.61	2.88	2.98	1.51	1.35	2.19	3.09	163.24	171.64	148.57	169.99	165.49	115.70
6	43.23	20.48	0.53	0.97	1.71	1.48	0.62	0.67	161.41	170.91	167.86	107.66	170.76	170.14
7	43.57	23.56	2.12	2.20	1.42	1.87	2.01	0.92	48.79	134.86	175.13	207.95	165.18	163.84
8	44.17	21.04	1.59	1.10	2.78	1.98	1.21	1.83	178.15	158.09	120.07	86.11	163.80	204.62
10	44.40	21.98	4.13	2.04	1.39	1.21	1.73	3.07	40.43	113.54	156.24	77.90	152.88	175.29
14	43.68	20.00	1.86	0.73	0.72	1.02	2.33	1.78	161.63	160.84	161.07	176.04	178.22	44.74
16	44.39	20.00	1.69	2.71	1.34	2.31	0.94	2.29	121.83	175.50	80.27	157.78	173.77	118.27

NOTE—Table 4 is published in its entirety in the machine-readable format. A portion is shown here for guidance regarding its form and content.

- Baloković, M., Brightman, M., Harrison, F. A., et al. 2018, *The Astrophysical Journal*, 854, 42, doi: [10.3847/1538-4357/aaa7eb](https://doi.org/10.3847/1538-4357/aaa7eb)
- Barthelmy, S. D., Barbier, L. M., Cummings, J. R., et al. 2005, *Space Science Reviews*, 120, 143, doi: [10.1007/s11214-005-5096-3](https://doi.org/10.1007/s11214-005-5096-3)
- Baumgartner, W. H., Tueller, J., Markwardt, C. B., et al. 2013, *ApJS*, 207, 19, doi: [10.1088/0067-0049/207/2/19](https://doi.org/10.1088/0067-0049/207/2/19)
- Bianchi, S., & Guainazzi, M. 2007, 924, 822, doi: [10.1063/1.2774948](https://doi.org/10.1063/1.2774948)
- Bierschenk, M., Ricci, C., Temple, M. J., et al. 2024, BASS XLI: The Correlation between Mid-infrared Emission Lines and Active Galactic Nuclei Emission, arXiv, doi: [10.48550/arXiv.2409.17334](https://doi.org/10.48550/arXiv.2409.17334)
- Brandt, W., & Hasinger, G. 2005, *Annual Review of Astronomy and Astrophysics*, 43, 827, doi: [10.1146/annurev.astro.43.051804.102213](https://doi.org/10.1146/annurev.astro.43.051804.102213)
- Brandt, W. N., & Alexander, D. M. 2015, *Astron Astrophys Rev*, 23, 1, doi: [10.1007/s00159-014-0081-z](https://doi.org/10.1007/s00159-014-0081-z)
- Brandt, W. N., Laor, A., & Wills, B. J. 2000, *The Astrophysical Journal*, 528, 637, doi: [10.1086/308207](https://doi.org/10.1086/308207)
- Brandt, W. N., & Yang, G. 2022, *Surveys of the Cosmic X-Ray Background*, 78, doi: [10.1007/978-981-16-4544-0_130-1](https://doi.org/10.1007/978-981-16-4544-0_130-1)
- Brightman, M., & Nandra, K. 2011, *Monthly Notices of the Royal Astronomical Society*, 413, 1206, doi: [10.1111/j.1365-2966.2011.18207.x](https://doi.org/10.1111/j.1365-2966.2011.18207.x)
- Brightman, M., Nandra, K., Salvato, M., et al. 2014, *Monthly Notices of the Royal Astronomical Society*, 443, 1999, doi: [10.1093/mnras/stu1175](https://doi.org/10.1093/mnras/stu1175)
- Brunner, H., Liu, T., Lamer, G., et al. 2022, *Astronomy and Astrophysics*, 661, A1, doi: [10.1051/0004-6361/202141266](https://doi.org/10.1051/0004-6361/202141266)
- Buchner, J., Georgakakis, A., Nandra, K., et al. 2015, *ApJ*, 802, 89, doi: [10.1088/0004-637X/802/2/89](https://doi.org/10.1088/0004-637X/802/2/89)
- Burlon, D., Ajello, M., Greiner, J., et al. 2011, *The Astrophysical Journal*, 728, 58, doi: [10.1088/0004-637X/728/1/58](https://doi.org/10.1088/0004-637X/728/1/58)
- Caglar, T., Burtscher, L., Brandl, B., et al. 2020, *Astronomy and Astrophysics*, 634, A114, doi: [10.1051/0004-6361/201936321](https://doi.org/10.1051/0004-6361/201936321)
- Caglar, T., Koss, M. J., Burtscher, L., et al. 2023, *The Astrophysical Journal*, 956, 60, doi: [10.3847/1538-4357/acf11b](https://doi.org/10.3847/1538-4357/acf11b)
- Casey, C. M., Kartaltepe, J. S., Drakos, N. E., et al. 2023, *ApJ*, 954, 31, doi: [10.3847/1538-4357/acc2bc](https://doi.org/10.3847/1538-4357/acc2bc)
- Cash, W. 1979, *The Astrophysical Journal*, 228, 939, doi: [10.1086/156922](https://doi.org/10.1086/156922)
- Ceca, R. D., Caccianiga, A., Severgnini, P., et al. 2008, *A&A*, 487, 119, doi: [10.1051/0004-6361:20079319](https://doi.org/10.1051/0004-6361:20079319)
- Civano, F., Marchesi, S., Comastri, A., et al. 2016, *ApJ*, 819, 62, doi: [10.3847/0004-637X/819/1/62](https://doi.org/10.3847/0004-637X/819/1/62)
- Cruise, M., Guainazzi, M., Aird, J., et al. 2024, *Nat Astron*, 1, doi: [10.1038/s41550-024-02416-3](https://doi.org/10.1038/s41550-024-02416-3)
- Czerny, B., Abrassart, A., Collin-Souffrin, S., & Dumont, A.-M. 2000, *AIP Conference Proceedings*, 510, 415, doi: [10.1063/1.1303243](https://doi.org/10.1063/1.1303243)
- den Brok, J. S., Koss, M. J., Trakhtenbrot, B., et al. 2022, *The Astrophysical Journal Supplement Series*, 261, 7, doi: [10.3847/1538-4365/ac5b66](https://doi.org/10.3847/1538-4365/ac5b66)
- Duras, F., Bongiorno, A., Ricci, F., et al. 2020, *A&A*, 636, A73, doi: [10.1051/0004-6361/201936817](https://doi.org/10.1051/0004-6361/201936817)
- Elvis, M. 2000, *The Astrophysical Journal*, 545, 63, doi: [10.1086/317778](https://doi.org/10.1086/317778)
- Elvis, M., Civano, F., Vignali, C., et al. 2009, *ApJS*, 184, 158, doi: [10.1088/0067-0049/184/1/158](https://doi.org/10.1088/0067-0049/184/1/158)

- Franca, F. L., Fiore, F., Comastri, A., et al. 2005, *ApJ*, 635, 864, doi: [10.1086/497586](https://doi.org/10.1086/497586)
- Fruscione, A., McDowell, J. C., Allen, G. E., et al. 2006, 6270, 62701V, doi: [10.1117/12.671760](https://doi.org/10.1117/12.671760)
- Gehrels, N. 1986, *The Astrophysical Journal*, 303, 336, doi: [10.1086/164079](https://doi.org/10.1086/164079)
- Giacconi, R., Rosati, P., Tozzi, P., et al. 2001, *The Astrophysical Journal*, 551, 624, doi: [10.1086/320222](https://doi.org/10.1086/320222)
- Gilli, R., Comastri, A., & Hasinger, G. 2007, *Astronomy and Astrophysics*, 463, 79, doi: [10.1051/0004-6361:20066334](https://doi.org/10.1051/0004-6361:20066334)
- Gilli, R., Norman, C., Calura, F., et al. 2022, *Astronomy and Astrophysics*, 666, A17, doi: [10.1051/0004-6361/202243708](https://doi.org/10.1051/0004-6361/202243708)
- Grogin, N. A., Kocevski, D. D., Faber, S. M., et al. 2011, *ApJS*, 197, 35, doi: [10.1088/0067-0049/197/2/35](https://doi.org/10.1088/0067-0049/197/2/35)
- Gupta, K. K., Ricci, C., Tortosa, A., et al. 2021, *Monthly Notices of the Royal Astronomical Society*, 504, 428, doi: [10.1093/mnras/stab839](https://doi.org/10.1093/mnras/stab839)
- Harrison, F. A., Craig, W. W., Christensen, F. E., et al. 2013, *ApJ*, 770, 103, doi: [10.1088/0004-637X/770/2/103](https://doi.org/10.1088/0004-637X/770/2/103)
- Hasinger, G. 2008, *A&A*, 490, 905, doi: [10.1051/0004-6361:200809839](https://doi.org/10.1051/0004-6361:200809839)
- Hickox, R. C., & Alexander, D. M. 2018, *Annual Review of Astronomy and Astrophysics*, 56, 625, doi: [10.1146/annurev-astro-081817-051803](https://doi.org/10.1146/annurev-astro-081817-051803)
- Hopkins, P. F., Hernquist, L., Cox, T. J., et al. 2006, *The Astrophysical Journal Supplement Series*, 163, 1, doi: [10.1086/499298](https://doi.org/10.1086/499298)
- Hornschemeier, A. E., Brandt, W. N., Garmire, G. P., et al. 2000, *ApJ*, 541, 49, doi: [10.1086/309431](https://doi.org/10.1086/309431)
- Ichikawa, K., Ricci, C., Ueda, Y., et al. 2017, *ApJ*, 835, 74, doi: [10.3847/1538-4357/835/1/74](https://doi.org/10.3847/1538-4357/835/1/74)
- Kalberla, P. M. W., Burton, W. B., Hartmann, D., et al. 2005, *A&A*, 440, 775, doi: [10.1051/0004-6361:20041864](https://doi.org/10.1051/0004-6361:20041864)
- Kawamuro, T., Ueda, Y., Tazaki, F., Terashima, Y., & Mushotzky, R. 2016, *ApJ*, 831, 37, doi: [10.3847/0004-637X/831/1/37](https://doi.org/10.3847/0004-637X/831/1/37)
- Kawamuro, T., Ricci, C., Imanishi, M., et al. 2022, *ApJ*, 938, 87, doi: [10.3847/1538-4357/ac8794](https://doi.org/10.3847/1538-4357/ac8794)
- Khedekar, S., Majumdar, S., & Das, S. 2010, *Phys. Rev. D*, 82, 041301, doi: [10.1103/PhysRevD.82.041301](https://doi.org/10.1103/PhysRevD.82.041301)
- Koss, M., Mushotzky, R., Baumgartner, W., et al. 2013, *ApJL*, 765, L26, doi: [10.1088/2041-8205/765/2/L26](https://doi.org/10.1088/2041-8205/765/2/L26)
- Koss, M., Mushotzky, R., Treister, E., et al. 2012, *The Astrophysical Journal*, 746, L22, doi: [10.1088/2041-8205/746/2/L22](https://doi.org/10.1088/2041-8205/746/2/L22)
- Koss, M., Mushotzky, R., Veilleux, S., & Winter, L. 2010, *The Astrophysical Journal*, 716, L125, doi: [10.1088/2041-8205/716/2/L125](https://doi.org/10.1088/2041-8205/716/2/L125)
- Koss, M., Mushotzky, R., Veilleux, S., et al. 2011, *ApJ*, 739, 57, doi: [10.1088/0004-637X/739/2/57](https://doi.org/10.1088/0004-637X/739/2/57)
- Koss, M., Trakhtenbrot, B., Ricci, C., et al. 2017, *The Astrophysical Journal*, 850, 74, doi: [10.3847/1538-4357/aa8ec9](https://doi.org/10.3847/1538-4357/aa8ec9)
- Koss, M. J., Romero-Cañizales, C., Baronchelli, L., et al. 2015, *The Astrophysical Journal*, 807, 149, doi: [10.1088/0004-637X/807/2/149](https://doi.org/10.1088/0004-637X/807/2/149)
- Koss, M. J., Assef, R., Baloković, M., et al. 2016, *ApJ*, 825, 85, doi: [10.3847/0004-637X/825/2/85](https://doi.org/10.3847/0004-637X/825/2/85)
- Koss, M. J., Blecha, L., Bernhard, P., et al. 2018, *Nature*, 563, 214, doi: [10.1038/s41586-018-0652-7](https://doi.org/10.1038/s41586-018-0652-7)
- Koss, M. J., Strittmatter, B., Lamperti, I., et al. 2021, *The Astrophysical Journal Supplement Series*, 252, 29, doi: [10.3847/1538-4365/abcbfe](https://doi.org/10.3847/1538-4365/abcbfe)
- Koss, M. J., Trakhtenbrot, B., Ricci, C., et al. 2022a, *The Astrophysical Journal Supplement Series*, 261, 1, doi: [10.3847/1538-4365/ac6c8f](https://doi.org/10.3847/1538-4365/ac6c8f)
- . 2022b, *ApJS*, 261, 6, doi: [10.3847/1538-4365/ac650b](https://doi.org/10.3847/1538-4365/ac650b)
- Koss, M. J., Ricci, C., Trakhtenbrot, B., et al. 2022c, *ApJS*, 261, 2, doi: [10.3847/1538-4365/ac6c05](https://doi.org/10.3847/1538-4365/ac6c05)
- LaMassa, S., Peca, A., Urry, C. M., et al. 2024, *The Astrophysical Journal*, 974, 235, doi: [10.3847/1538-4357/ad6e7d](https://doi.org/10.3847/1538-4357/ad6e7d)
- LaMassa, S. M., Urry, C. M., Glikman, E., et al. 2013a, *Monthly Notices of the Royal Astronomical Society*, 432, 1351, doi: [10.1093/mnras/stt553](https://doi.org/10.1093/mnras/stt553)
- LaMassa, S. M., Urry, C. M., Cappelluti, N., et al. 2013b, *Monthly Notices of the Royal Astronomical Society*, 436, 3581, doi: [10.1093/mnras/stt1837](https://doi.org/10.1093/mnras/stt1837)
- Lansbury, G. B., Alexander, D. M., Aird, J., et al. 2017, *ApJ*, 846, 20, doi: [10.3847/1538-4357/aa8176](https://doi.org/10.3847/1538-4357/aa8176)
- Lanzuisi, G., Civano, F., Marchesi, S., et al. 2018, *Monthly Notices of the Royal Astronomical Society*, 480, 2578, doi: [10.1093/mnras/sty2025](https://doi.org/10.1093/mnras/sty2025)
- Liu, T., Tozzi, P., Wang, J.-X., et al. 2017, *ApJS*, 232, 8, doi: [10.3847/1538-4365/aa7847](https://doi.org/10.3847/1538-4365/aa7847)
- Liu, T., Buchner, J., Nandra, K., et al. 2022, *Astronomy and Astrophysics*, 661, A5, doi: [10.1051/0004-6361/202141643](https://doi.org/10.1051/0004-6361/202141643)
- Liu, Z., Merloni, A., Georgakakis, A., et al. 2016, *Monthly Notices of the Royal Astronomical Society*, 459, 1602, doi: [10.1093/mnras/stw753](https://doi.org/10.1093/mnras/stw753)
- Madau, P., & Dickinson, M. 2014, *Annual Review of Astronomy and Astrophysics*, 52, 415, doi: [10.1146/annurev-astro-081811-125615](https://doi.org/10.1146/annurev-astro-081811-125615)
- Madsen, K. K., García, J. A., Stern, D., et al. 2024, *Front. Astron. Space Sci.*, 11, doi: [10.3389/fspas.2024.1357834](https://doi.org/10.3389/fspas.2024.1357834)

- Marchesi, S., Ajello, M., Marcotulli, L., et al. 2018, *The Astrophysical Journal*, 854, 49, doi: [10.3847/1538-4357/aaa410](https://doi.org/10.3847/1538-4357/aaa410)
- Marchesi, S., Civano, F., Elvis, M., et al. 2016a, *The Astrophysical Journal*, 817, 34, doi: [10.3847/0004-637X/817/1/34](https://doi.org/10.3847/0004-637X/817/1/34)
- Marchesi, S., Lanzuisi, G., Civano, F., et al. 2016b, *The Astrophysical Journal*, 830, 100, doi: [10.3847/0004-637X/830/2/100](https://doi.org/10.3847/0004-637X/830/2/100)
- Marchesi, S., Gilli, R., Lanzuisi, G., et al. 2020, *A&A*, 642, A184, doi: [10.1051/0004-6361/202038622](https://doi.org/10.1051/0004-6361/202038622)
- Matthee, J., Naidu, R. P., Brammer, G., et al. 2024, *ApJ*, 963, 129, doi: [10.3847/1538-4357/ad2345](https://doi.org/10.3847/1538-4357/ad2345)
- McKaig, J., Ricci, C., Paltani, S., et al. 2023, *Monthly Notices of the Royal Astronomical Society*, 526, 5072, doi: [10.1093/mnras/stad2974](https://doi.org/10.1093/mnras/stad2974)
- Mejía-Restrepo, J. E., Trakhtenbrot, B., Koss, M. J., et al. 2022, *ApJS*, 261, 5, doi: [10.3847/1538-4365/ac6602](https://doi.org/10.3847/1538-4365/ac6602)
- Menzel, M. L., Merloni, A., Georgakakis, A., et al. 2016, *Monthly Notices of the Royal Astronomical Society*, 457, 110, doi: [10.1093/mnras/stv2749](https://doi.org/10.1093/mnras/stv2749)
- Morrison, R., & McCammon, D. 1983, *The Astrophysical Journal*, 270, 119, doi: [10.1086/161102](https://doi.org/10.1086/161102)
- Murphy, K. D., & Yaqoob, T. 2009, *Monthly Notices of the Royal Astronomical Society*, 397, 1549, doi: [10.1111/j.1365-2966.2009.15025.x](https://doi.org/10.1111/j.1365-2966.2009.15025.x)
- Nandra, K., Barret, D., Barcons, X., et al. 2013, *The Hot and Energetic Universe: A White Paper Presenting the Science Theme Motivating the Athena+ Mission*, doi: [10.48550/arXiv.1306.2307](https://doi.org/10.48550/arXiv.1306.2307)
- Nandra, K., Waddell, S. G. H., Liu, T., et al. 2024, *The eROSITA Final Equatorial Depth Survey (eFEDS): The Hard X-ray Selected Sample*, doi: [10.48550/arXiv.2401.17300](https://doi.org/10.48550/arXiv.2401.17300)
- Oh, K., Koss, M., Markwardt, C. B., et al. 2018, *The Astrophysical Journal Supplement Series*, 235, 4, doi: [10.3847/1538-4365/aaa7fd](https://doi.org/10.3847/1538-4365/aaa7fd)
- Oh, K., Koss, M. J., Ueda, Y., et al. 2022, *ApJS*, 261, 4, doi: [10.3847/1538-4365/ac5b68](https://doi.org/10.3847/1538-4365/ac5b68)
- Peca, A., Cappelluti, N., Marchesi, S., Hodges-Kluck, E., & Foord, A. 2024, *Universe*, 10, 245, doi: [10.3390/universe10060245](https://doi.org/10.3390/universe10060245)
- Peca, A., Vignali, C., Gilli, R., et al. 2021, *The Astrophysical Journal*, 906, 90, doi: [10.3847/1538-4357/abc9c7](https://doi.org/10.3847/1538-4357/abc9c7)
- Peca, A., Cappelluti, N., Urry, C. M., et al. 2023, *The Astrophysical Journal*, 943, 162, doi: [10.3847/1538-4357/acac28](https://doi.org/10.3847/1538-4357/acac28)
- Pfeifle, R. W., Ricci, C., Boorman, P. G., et al. 2022, *ApJS*, 261, 3, doi: [10.3847/1538-4365/ac5b65](https://doi.org/10.3847/1538-4365/ac5b65)
- Predehl, P., Andritschke, R., Arefiev, V., et al. 2021, *Astronomy and Astrophysics*, 647, A1, doi: [10.1051/0004-6361/202039313](https://doi.org/10.1051/0004-6361/202039313)
- Reynolds, C. S. 1999, 161, 178, doi: [10.48550/arXiv.astro-ph/9810018](https://doi.org/10.48550/arXiv.astro-ph/9810018)
- Reynolds, C. S., Kara, E. A., Mushotzky, R. F., et al. 2023, 12678, 126781E, doi: [10.1117/12.2677468](https://doi.org/10.1117/12.2677468)
- Ricci, C., Ueda, Y., Koss, M. J., et al. 2015, *ApJ*, 815, L13, doi: [10.1088/2041-8205/815/1/L13](https://doi.org/10.1088/2041-8205/815/1/L13)
- Ricci, C., Trakhtenbrot, B., Koss, M. J., et al. 2017a, *Nature*, 549, 488, doi: [10.1038/nature23906](https://doi.org/10.1038/nature23906)
- Ricci, C., Bauer, F. E., Treister, E., et al. 2017b, *Monthly Notices of the Royal Astronomical Society*, 468, 1273, doi: [10.1093/mnras/stx173](https://doi.org/10.1093/mnras/stx173)
- Ricci, C., Trakhtenbrot, B., Koss, M. J., et al. 2017c, *ApJS*, 233, 17, doi: [10.3847/1538-4365/aa96ad](https://doi.org/10.3847/1538-4365/aa96ad)
- Ricci, C., Privon, G. C., Pfeifle, R. W., et al. 2021, *Monthly Notices of the Royal Astronomical Society*, 506, 5935, doi: [10.1093/mnras/stab2052](https://doi.org/10.1093/mnras/stab2052)
- Ricci, C., Ananna, T. T., Temple, M. J., et al. 2022, *ApJ*, 938, 67, doi: [10.3847/1538-4357/ac8e67](https://doi.org/10.3847/1538-4357/ac8e67)
- Ricci, C., Ichikawa, K., Stalevski, M., et al. 2023a, *The Astrophysical Journal*, 959, 27, doi: [10.3847/1538-4357/ad0733](https://doi.org/10.3847/1538-4357/ad0733)
- Ricci, C., Chang, C.-S., Kawamuro, T., et al. 2023b, *ApJL*, 952, L28, doi: [10.3847/2041-8213/acda27](https://doi.org/10.3847/2041-8213/acda27)
- Scoville, N., Aussel, H., Brusa, M., et al. 2007, *ApJS*, 172, 1, doi: [10.1086/516585](https://doi.org/10.1086/516585)
- Signorini, M., Marchesi, S., Gilli, R., et al. 2023, *Astronomy and Astrophysics*, 676, A49, doi: [10.1051/0004-6361/202346364](https://doi.org/10.1051/0004-6361/202346364)
- Simmonds, C., Buchner, J., Salvato, M., Hsu, L. T., & Bauer, F. E. 2018, *Astronomy and Astrophysics*, 618, A66, doi: [10.1051/0004-6361/201833412](https://doi.org/10.1051/0004-6361/201833412)
- Smith, K. L., Mushotzky, R. F., Koss, M., et al. 2020, *Monthly Notices of the Royal Astronomical Society*, 492, 4216, doi: [10.1093/mnras/stz3608](https://doi.org/10.1093/mnras/stz3608)
- Tanimoto, A., Ueda, Y., Odaka, H., Yamada, S., & Ricci, C. 2022, *The Astrophysical Journal Supplement Series*, 260, 30, doi: [10.3847/1538-4365/ac5f59](https://doi.org/10.3847/1538-4365/ac5f59)
- Tozzi, P., Gilli, R., Mainieri, V., et al. 2006, *Astronomy and Astrophysics*, Volume 451, Issue 2, May IV 2006, pp.457-474, 451, 457, doi: [10.1051/0004-6361:20042592](https://doi.org/10.1051/0004-6361:20042592)
- Treister, E., & Urry, C. M. 2006, *The Astrophysical Journal*, 652, L79, doi: [10.1086/510237](https://doi.org/10.1086/510237)
- Treister, E., Urry, C. M., & Virani, S. 2009, *The Astrophysical Journal*, 696, 110, doi: [10.1088/0004-637X/696/1/110](https://doi.org/10.1088/0004-637X/696/1/110)

- Ueda, Y., Akiyama, M., Hasinger, G., Miyaji, T., & Watson, M. G. 2014, *The Astrophysical Journal*, 786, 104, doi: [10.1088/0004-637X/786/2/104](https://doi.org/10.1088/0004-637X/786/2/104)
- Ueda, Y., Eguchi, S., Terashima, Y., et al. 2007, *The Astrophysical Journal*, 664, L79, doi: [10.1086/520576](https://doi.org/10.1086/520576)
- Urry, C. 2004, in *AGN Physics with the Sloan Digital Sky Survey*, Vol. 311, eprint: arXiv:astro-ph/0312545, 49, doi: [10.48550/arXiv.astro-ph/0312545](https://doi.org/10.48550/arXiv.astro-ph/0312545)
- Wilson, A. S., & Colbert, E. J. M. 1995, *The Astrophysical Journal*, 438, 62, doi: [10.1086/175054](https://doi.org/10.1086/175054)
- Yaqoob, T. 1997, *The Astrophysical Journal*, 479, 184, doi: [10.1086/303843](https://doi.org/10.1086/303843)